A Novel Transformation of the Ice Sheet Stokes Equations and Some of its Properties and Applications

John K. Dukowicz

Guest Scientist, Group T-3, Los Alamos National Laboratory,

Los Alamos, New Mexico, 87545, USA

Correspondence to: John K. Dukowicz (jn.dk@outlook.com)

Abstract.   We introduce a novel transformation of the Stokes equations into a form closely resembling the shallow Blatter-Pattyn equations. The two forms differ by only a few additional terms, while their variational formulations differ only by a single term in each horizontal direction. Specifically, the variational formulation of the Blatter-Pattyn model drops the vertical velocity in the second invariant of the strain rate tensor. Here we make use of the new transformation in two ways. First, we consider incorporating the transformed equations into a code that can be very easily converted from a Stokes to a Blatter-Pattyn model, and vice-versa, by switching these terms on or off. This may be generalized so that the Stokes model is switched on adaptively only where the Blatter-Pattyn model loses accuracy. Second, the key role played by the vertical velocity in the Blatter-Pattyn approximation motivates new approximations. Two examples are presented. These require a mesh that enables the discrete continuity equation to be invertible for the vertical velocity in terms of the horizontal velocity components. Examples of such meshes, such as the first order P1-E0 mesh and the second order P2-E1 mesh are given in both 2D and 3D. However, the transformed Stokes model has the same type of gravity forcing as the Blatter-Pattyn model, determined by the ice surface slope, thereby forgoing some of the mesh-generality of the traditional formulation of the Stokes model.

1 Introduction

Concern and uncertainty about the magnitude of sea level rise due to melting of the Greenland and Antarctic ice sheets have led to increased interest in improved ice sheet and glacier modeling. The gold standard is a Stokes model (i.e., a model that solves the nonlinear, non-Newtonian Stokes system of equations for incompressible ice sheet dynamics) because it is applicable to all geometries and flow regimes. However, the Stokes model is computationally demanding. It is a nonlinear, three-dimensional model involving four variables, namely, the three velocity components and pressure. The pressure is a Lagrange multiplier enforcing incompressibility and this creates a more

June 20, 2025

38   difficult indefinite "saddle point" problem. As a result, full-Stokes models exist but are

39   not commonly used in practice (examples are FELIX-S, Leng et al., 2012; Elmer/Ice,

40   Gagliardini et al., 2013).

42   Because of this there is much interest in simpler and cheaper approximate models.

43   There is a hierarchy of very simple models, such as the shallow ice (SIA) and shallow-

44   shelf (SSA) models, and there are also more accurate higher-order approximations.

45   These culminate in the Blatter-Pattyn (BP) approximation (Blatter, 1995; Pattyn, 2003),

46   which is currently used in production code packages such as ISSM (Larour et al., 2012),

47   MALI (Hoffman et al., 2018; Tezaur et al., 2015) and CISM (Lipscomb et al., 2019).

48   This approximation is based on the assumption of a small ice sheet aspect ratio, i.e.,

49    $\varepsilon = H/L \ll 1$, where H, L are the vertical and horizontal length scales, and consequently

50   it eliminates certain stress terms and implicitly assumes small basal slopes. Both the

51   Stokes and Blatter-Pattyn models are described in detail in Dukowicz et al. (2010),

52   hereafter referred to as DPL (2010). Although the Blatter-Pattyn model is reasonably

53   accurate for large-scale motions, accuracy deteriorates for small horizontal scales, less

54   than about five ice thicknesses in the ISMIP–HOM model intercomparison (Pattyn et al.,

55   2008; Perego et al., 2012), or below a 1 km resolution as found in a detailed comparison

56   with full Stokes calculations (Rückamp et al, 2022). This can become particularly

57   important for calculations involving details near the grounding line where the full

58   accuracy of the Stokes model is needed (Nowicki and Wingham, 2008). Attempts to

59   address the problem while avoiding the use of full Stokes solvers include variable mesh

60   resolution coupled with a Blatter-Pattyn solver (Hoffman et al., 2018) and variable model

61   complexity, where a Stokes solver is embedded locally in a lower order model (Seroussi

62   et al., 2012). Approximations that are more accurate than Blatter-Pattyn but cheaper than

63   Stokes are currently not available.

64

65   The present paper introduces two innovations that may begin to address some of

66   these issues. The first is a novel transformation of the Stokes model, described in §3,

67   which puts it into a form closely resembling the Blatter-Pattyn model and differing only

68   by the presence of a few extra terms. This allows a code to be switched over from Stokes

69   to Blatter-Pattyn, and vice-versa, globally or locally, by the use of a single parameter that

70   turns off these extra terms thus enabling variable model complexity to be very simply

71   implemented as described in §6.1. The second innovation is the introduction of new

June 20, 2025

72 finite element discretizations that decouple the discrete continuity equation and allow it to

73 be solved for the vertical velocity in terms of the horizontal velocity components.

74 Several elements used to construct such meshes are described in Appendix A in both 2D

75 and 3D, primarily the first order P1-E0 and second order P2-E1 elements (these two

76 elements are novel and are so-named because they employ pressures located on vertical

77 mesh edges). Within the framework of the transformed Stokes model these meshes

78 enable new approximations that surpass the Blatter-Pattyn approximation. We describe

79 two such approximations in §6.2. There is another very significant benefit. These new

80 meshes allow Stokes ice sheet models to be converted into inherently stable

81 unconstrained minimization problems without invoking the "inf-sup" condition as shown

82 in §4.3.2.

83

84 **2 The Standard Formulation of the Stokes Ice Sheet Model**

85 **2.1 The Assumed Ice Sheet Configuration**

86

87 An ice sheet may be divided into two parts, a part in contact with the bed and a floating

88 ice shelf located beyond the grounding line. The Stokes ice sheet model is capable of

89 describing the flow of an arbitrarily shaped ice sheet, including a floating ice shelf as

90 illustrated in Fig. 1, given appropriate boundary conditions (e.g., Cheng et al., 2020).

91 One limitation of the methods proposed here, in common with the Blatter-Pattyn model,

92 will be that there should be just one upper and one basal surface, as is the case in Fig. 1.

93 For simplicity we only consider fully grounded ice sheets with periodic lateral boundary

94 conditions although ice shelves can be incorporated.
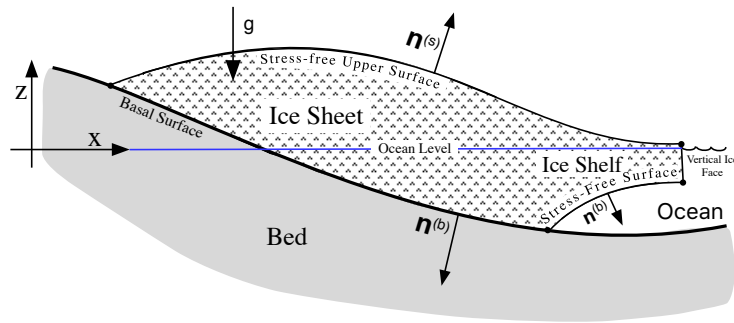
95
96
97 **Figure 1** A simplified illustration of the admissible ice sheet configuration.

98

99   Referring to Fig. 1, the entire surface of the ice sheet is denoted by S. An upper

100   surface, labeled S_s and specified by $\varsigma_s(x,y,z)=z-z_s(x,y)=0$, is exposed to the

101   atmosphere and thus experiences stress-free boundary conditions. The bottom or basal

102   surface, denoted by S_B and specified by $\varsigma_b(x,y,z)=z-z_b(x,y)=0$, is in contact with

103   the bed. The basal surface may be subdivided into two sections, $S_B=S_{B1}\cup S_{B2}$, where

104   S_{B1}, specified by $z=z_{b1}(x,y)$, is the part where ice is frozen to the bed (a no-slip

105   boundary condition), and S_{B2}, specified by $z=z_{b2}(x,y)$, is where frictional sliding

106   occurs. We assume Cartesian coordinates such that $x_i=(x,y,z)$ are position coordinates

107   with $z=0$ at the ocean surface, and the index $i\in\{x,y,z\}$ represents the three Cartesian

108   indices. Later we shall have occasion to introduce the restricted index $(i)\in\{x,y\}$ to

109   represent just the two horizontal indices. This is more compact than the equivalent

110   projection operator, i.e., $u_{(i)}=P_i(u)=(u,v,0)$. Unit normal vectors appropriate for the

111   ice sheet configuration of Fig. 1 are given by

112
$$n_i=(n_x,n_y,n_z)=\frac{\partial\varsigma_s(x,y,z)/\partial x_i}{\left|\partial\varsigma_s(x,y,z)/\partial x_i\right|}=\frac{(-\partial z_s/\partial x,-\partial z_s/\partial y,1)}{\sqrt{1+(\partial z_s/\partial x)^2+(\partial z_s/\partial y)^2}} \qquad \text{at surface } S_S,$$

$$n_i=(n_x,n_y,n_z)=-\frac{\partial\varsigma_b(x,y,z)/\partial x_i}{\left|\partial\varsigma_b(x,y,z)/\partial x_i\right|}=\frac{(\partial z_b/\partial x,\partial z_b/\partial y,-1)}{\sqrt{1+(\partial z_b/\partial x)^2+(\partial z_b/\partial y)^2}} \qquad \text{at surface } S_B.$$

(1)

113

114   **2.2 The Stokes Equations**

115

116   The Stokes model is a system of nonlinear partial differential equations and associated

117   boundary conditions (Greve and Blatter, 2009; DPL, 2010). In Cartesian coordinates the

118   Stokes equations, the three momentum equations and the continuity equation for the three

119   velocity components $u_i=(u,v,w)$ and the pressure P, are given by

120
$$\frac{\partial\tau_{ij}}{\partial x_j}-\frac{\partial P}{\partial x_i}+\rho g_i=0,$$
(2)

121
$$\frac{\partial u_i}{\partial x_i}=0,$$
(3)

June 20, 2025

122   where ρ is the density, and g_i is the acceleration vector due to gravity, arbitrarily

123   oriented in general but here taken to be in the negative z-direction, $g_i = (0,0,-g)$.

124   Repeated indices imply summation (the Einstein notation). The deviatoric stress tensor

125   τ_{ij} is given by

$$\tau_{ij} = 2\mu_n \dot{\varepsilon}_{ij}, \tag{4}$$

127   where the strain rate tensor is

$$\dot{\varepsilon}_{ij} = \frac{1}{2}\left(\frac{\partial u_i}{\partial x_j} + \frac{\partial u_j}{\partial x_i}\right), \tag{5}$$

129   the nonlinear ice viscosity μ_n is

$$\mu_n = \eta_0 \left(\dot{\varepsilon}^2\right)^{(1-n)/2n}, \tag{6}$$

131   and $\dot{\varepsilon}^2 = \dot{\varepsilon}_{ij}\dot{\varepsilon}_{ij}/2 \geq 0$ is the second invariant of the strain rate tensor that may be written

132   out in full as follows

$$\dot{\varepsilon}^2 = \frac{1}{2}\left[\left(\frac{\partial u}{\partial x}\right)^2 + \left(\frac{\partial v}{\partial y}\right)^2 + \left(\frac{\partial w}{\partial z}\right)^2\right] + \frac{1}{4}\left[\left(\frac{\partial u}{\partial y} + \frac{\partial v}{\partial x}\right)^2 + \left(\frac{\partial u}{\partial z} + \frac{\partial w}{\partial x}\right)^2 + \left(\frac{\partial v}{\partial z} + \frac{\partial w}{\partial y}\right)^2\right]. \tag{7}$$

134   As usual, ice is assumed to obey Glen's flow law, where n is the Glen's law exponent

135   ($n = 1$ for a linear Newtonian fluid but typically $n = 3$ in ice sheet modeling, describing a

136   nonlinear non-Newtonian fluid). The coefficient η_0 is defined by $\eta_0 = A^{-1/n}/2$, where

137   A is an ice flow factor, in general depending on temperature and other variables (see

138   Schoof and Hewitt, 2013) but here taken to be a constant. The three-dimensional Stokes

139   system requires a set of boundary conditions at every bounding surface, each set

140   composed of three components. Aside from the periodic lateral boundary conditions, the

141   relevant boundary conditions are given as follows

142   (1) Stress-free boundary conditions on surfaces S_S not in contact with the bed, such

143   as the upper surface S_S:

$$\tau_{ij}n_j - Pn_t = 0. \tag{8}$$

145   (2) No-slip or frozen to the bed conditions on surface segment S_{B1}:

$$u_i = 0. \tag{9}$$

147   (3) Frictional tangential sliding conditions on surface segment S_{B2}:

June 20, 2025

148   We assume that the tangential frictional shear force that resists sliding, τ_i^S, is a known

149   vector that satisfies the no-penetration condition, $\tau_i^S n_i = 0$. Note that only two

150   components need to be provided since the third may always be obtained from the

151   tangency condition. In general τ_i^S is a complicated function of position and velocity

152   (e.g., Schoof, 2010). At a surface where frictional sliding takes place the flow velocity

153   must be tangential to the surface, satisfying

154 $$u_i n_i = 0. \tag{10}$$

155   Following DPL (2010), the tangential stress balance at the basal surface is given by

156 $$\tau_{ij} n_j - \tau_n n_i + \tau_i^S = 0, \tag{11}$$

157   where $\tau_n = n_i \tau_{ij} n_j$ is the normal component of the shear stress. However, the three

158   components of the stress balance (11) are not independent since the stress balance vector

159   is confined to the tangential plane. Thus, choosing the horizontal components of (11) as

160   the two independent components, the required three boundary conditions are given by the

161   no-penetration condition (10) and the two horizontal components of (11), namely

162 $$\tau_{(i)j} n_j - \tau_n n_{(i)} + \tau_{(i)}^S = 0. \tag{12}$$

163   In this paper we shall assume simple linear frictional sliding, given by

164 $$\tau_i^S = \beta(x) u_i, \tag{13}$$

165   where $\beta(x) > 0$ is a position-dependent drag law coefficient. We also assume that there

166   is no melting or refreezing at the bed, causing vertical inflows or outflows. If needed,

167   these can be easily added to (10) (see Dukowicz et al., 2010; Heinlein et al., 2022).

168

169   **2.3 The Stokes Variational Principle**

170

171   A variational principle, if available, is the most compact way of representing a particular

172   problem. It is fortunate that the Stokes model possesses a variational principle that is

173   particularly useful for discretization and for the specification of boundary conditions (see

174   Colinge and Rappaz (1999), Glowinski and Rappaz (2003), Rappaz and Reist (2005) for

175   early use of the variational principle in glaciology, and Schoof (2006), DPL (2010) for a

176   fuller description of the variational principle as applied in ice sheet modeling). There are

177   a number of significant advantages. For example, all boundary conditions are

178   conveniently incorporated in the variational formulation, terms in the variational

June 20, 2025

179 functional generally contain lower order derivatives, and the discretization automatically
180 generates a symmetric matrix. Stress terms are evaluated in the interior thereby avoiding
181 the need to evaluate derivatives using less accurate one-sided approximations at
182 boundaries. Stress-free boundary conditions, as at the upper surface, need not be
183 specified at all since they are automatically incorporated in the functional as natural
184 boundary conditions. Finally, functional variation in the discrete case is equivalent to
185 simple differentiation with respect to the discrete variables as demonstrated in §4. The
186 variational method presented here is closely related to the Galerkin method, a subset of
187 the weak formulation method in finite elements in which the test and trial functions are
188 the same (see Schoof, 2010, and earlier references contained therein in connection with
189 the Blatter-Pattyn model).

190

191 The variational functional for the standard Stokes model may be written in two
192 alternative forms:

193 (1) Basal boundary conditions imposed using Lagrange multipliers:

194
$$\mathcal{A}[u_i, P, \lambda_i, \Lambda] = \int_V dV \left[\frac{4n}{n+1} \eta_0 \left(\dot{\varepsilon}^2 \right)^{(1+n)/2n} - P \frac{\partial u_i}{\partial x_i} + \rho g w \right]$$
$$+ \int_{S_{B1}} dS \, \lambda_i u_i + \int_{S_{B2}} dS \left[\Lambda u_i n_i + \frac{1}{2} \beta(x) \, u_i u_i \right], \tag{14}$$

195 where λ_i and Λ are Lagrange multipliers used to enforce the no-slip condition and
196 frictional tangential sliding, respectively. As in DPL (2010), arguments enclosed in
197 square brackets, here $u_i, P, \lambda_i, \Lambda$, indicates the functions that are subject to variation.

198 (2) Basal boundary conditions imposed by direct substitution:
199 In case of no-slip conditions, condition (9) is used directly in the functional to zero out all
200 velocity components u_i along the S_{B1} section of the basal boundary. In case of
201 tangential sliding, the functional is given by

202
$$\mathcal{A}[u_i, P] = \int_V dV \left[\frac{4n}{n+1} \eta_0 \left(\dot{\varepsilon}^2 \right)^{(1+n)/2n} - P \frac{\partial u_i}{\partial x_i} + \rho g w \right]$$
$$+ \frac{1}{2} \int_{S_{B2}} dS \, \beta(x) \left(u_{(i)} u_{(i)} + \left(u_{(i)} n_{(i)} / n_z \right)^2 \right), \tag{15}$$

203 where, using the tangential sliding condition (10), the velocity along the entire basal
204 boundary section S_{B2} is specified by

205
$$u_i = \left(u, v, -u_{(i)} n_{(i)} / n_z \right) = \left(u, v, u_{(i)} \, \partial z_b / \partial x_{(i)} \right).$$
(16)

206 This is implicitly done in all terms of the functional, i.e., the volume integral terms as
207 well as the surface integral term, in which case the replacement is explicitly visible in
208 (15). This use of (16) to replace the relevant surface velocities in the functional is
209 sufficient to implement the tangential sliding boundary condition. The replacement is
210 particularly easy in the discrete formulation, to be described later, where boundary or
211 surface velocity variables are easily accessible for replacement.
212
213   As fully described in DPL (2010), a variational procedure yields the full set of
214 Euler-Lagrange equations and boundary conditions that specify the standard Stokes
215 model, equivalent to (2)-(12). In the case of (14), the discrete variational procedure
216 determines the discrete variables that specify the velocity components and the pressure,
217 u_i, P, and the Lagrange multipliers, λ_i, Λ. In the direct substitution case, (15), the
218 solution determines only the discrete pressures P and velocity variables u_i that were not
219 directly prescribed as boundary conditions in (9) or (16). These prescribed (known)
220 values of boundary velocities are then added a posteriori to obtain the complete set of
221 discrete variables. The direct substitution method is smaller, simpler, and is therefore
222 more commonly used in this paper.
223
224 **3. A Transformation of the Stokes Model**
225 **3.1 Origin of the Transformation**
226
227 The transformation is motivated by the Blatter-Pattyn approximation. Consider the
228 vertical component of the momentum equation and the corresponding stress-free upper
229 surface boundary condition in the Blatter-Pattyn approximation (from DPL, 2010, for
230 example), which are given by

231
$$\frac{\partial}{\partial z}\left(2\mu_n \frac{\partial w}{\partial z} \right) - \frac{\partial P}{\partial z} - \rho g = 0,$$
$$\left(2\mu_n \frac{\partial w}{\partial z} - P \right) n_z = 0 \quad \text{at} \quad z = z_s(x,y).$$
(17)

232 These equations suggest the use of a new variable $\tilde{P}$, to be called the transformed
233 pressure, given by

June 20, 2025

234
$$\tilde{P} = P - 2\mu_n \frac{\partial w}{\partial z} + \rho g\left(z - z_s(x, y)\right). \tag{18}$$

235 Substituting, this simplifies (17) as follows

236
$$\frac{\partial \tilde{P}}{\partial z} = 0, \tag{19}$$
$$\tilde{P} n_z = 0 \quad \text{at} \quad z = z_s(x, y),$$

237 which is a complete one-dimensional partial differential system yielding

238
$$\tilde{P} = 0 \tag{20}$$

239 when integrated from the top surface down. Thus, the transformed pressure vanishes in
240 the Blatter-Pattyn case. The definition (18) forms the basis of the present transformation
241 but we also use the continuity equation to eliminate $\partial w/\partial z$ as in the Blatter-Pattyn
242 approximation (e.g., Pattyn, 2003). Therefore, the transformation consists of eliminating
243 P and $\partial w/\partial z$ in the Stokes system (2), (4)-(12) (i.e., everywhere except in the
244 continuity equation (3) itself) by means of

245
$$P = \tilde{P} - 2\mu_n\left(\frac{\partial u}{\partial x} + \frac{\partial v}{\partial y}\right) + \rho g\left(z_s - z\right), \tag{21}$$

246
$$\frac{\partial w}{\partial z} = -\left(\frac{\partial u}{\partial x} + \frac{\partial v}{\partial y}\right). \tag{22}$$

247
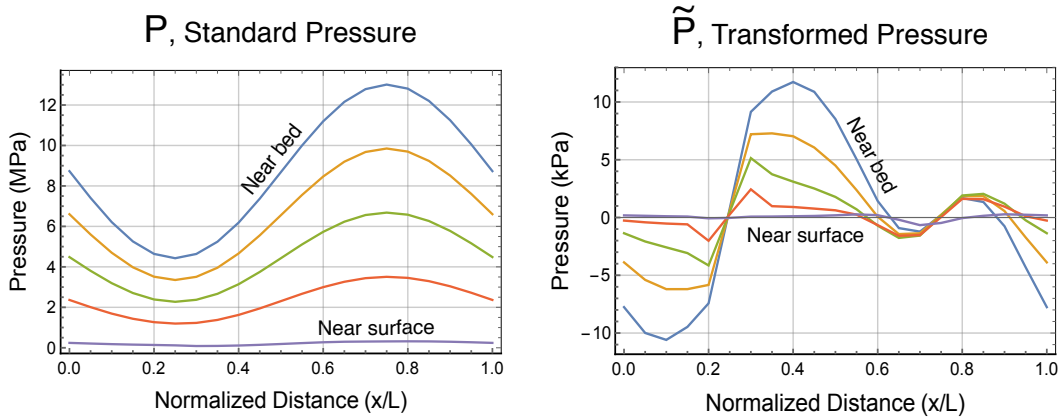
248 **Figure 2.** Standard pressure P (MPa) compared to the transformed pressure $\tilde{P}$ (kPa) in
249 Exp. B from the ISMIP–HOM model intercomparison (Pattyn et al., 2008) at L = 10 km.

250

251 The pressure P in the standard Stokes system is primarily a Lagrange multiplier
252 enforcing incompressibility, but with a very large hydrostatic component. The
253 transformation eliminates the hydrostatic pressure from $\tilde{P}$, as illustrated in Fig. 2 where

June 20, 2025

254   the two pressures are compared. Thus, the transformed pressure $\tilde{P}$ is some three orders

255   of magnitude smaller than P primarily because of the absence of hydrostatic pressure.

256

257   The transformed pressure $\tilde{P}$ again acts as a Lagrange multiplier enforcing

258   incompressibility. Since $\tilde{P}=0$ in the Blatter-Pattyn approximation, the transformed

259   pressure may be written as $\tilde{P}=P-P_{BP}$, where

260
$$P_{BP}=-2\mu_n\left(\frac{\partial u}{\partial x}+\frac{\partial v}{\partial y}\right)+\rho g\left(z_s-z\right)$$

261   is the effective Blatter-Pattyn pressure (Tezaur et al., 2015). Thus, $P=P_{BP}+\tilde{P}$ and

262   therefore $\tilde{P}$ can be interpreted as the "Stokes" correction to the Blatter-Pattyn pressure.

263

264   **3.2 The Transformed Stokes Equations**

265

266   Introducing (21), (22) into the Stokes system of equations (2)-(12) results in the

267   following transformed Stokes system:

268
$$\frac{\partial\tilde{\tau}_{ij}}{\partial x_j}-\hat{\xi}\frac{\partial\tilde{P}}{\partial x_i}-\rho g\frac{\partial z_s}{\partial x_{(i)}}=0\,,\tag{23}$$

269
$$\hat{\xi}\frac{\partial u_i}{\partial x_i}=0\,,\tag{24}$$

270   where quantities modified in the transformation are indicated by a tilde, e.g., $\tilde{P}$.

271   Corresponding to (4), the modified Stokes deviatoric stress tensor $\tilde{\tau}_{ij}$ is given by

272
$$\tilde{\tau}_{ij}=\tilde{\mu}_n\begin{bmatrix}2\left(2\dfrac{\partial u}{\partial x}+\dfrac{\partial v}{\partial y}\right)&\left(\dfrac{\partial u}{\partial y}+\dfrac{\partial v}{\partial x}\right)&\left(\dfrac{\partial u}{\partial z}+\xi\dfrac{\partial w}{\partial x}\right)\\[2ex]\left(\dfrac{\partial u}{\partial y}+\dfrac{\partial v}{\partial x}\right)&2\left(\dfrac{\partial u}{\partial x}+2\dfrac{\partial v}{\partial y}\right)&\left(\dfrac{\partial v}{\partial z}+\xi\dfrac{\partial w}{\partial y}\right)\\[2ex]\xi\left(\dfrac{\partial u}{\partial z}+\dfrac{\partial w}{\partial x}\right)&\xi\left(\dfrac{\partial v}{\partial z}+\dfrac{\partial w}{\partial y}\right)&0\end{bmatrix}\,,\tag{25}$$

273   Dummy variables $\xi,\hat{\xi}$ (here assumed to be $\xi,\hat{\xi}=1$) are used in (23)-(25) to indicate

274   terms that are absent in the Blatter-Blatter approximation as will be explained below.

275   The modified viscosity $\tilde{\mu}_n$, corresponding to (6), is given by

June 20, 2025

276
$$\tilde{\mu}_n = \eta_0 \left(\tilde{\dot{\varepsilon}}^2 \right)^{(1-n)/2n} , \qquad (26)$$

277 where the transformed second invariant $\tilde{\dot{\varepsilon}}^2$, corresponding to (7), is

278
$$\tilde{\dot{\varepsilon}}^2 = \left(\frac{\partial u}{\partial x} \right)^2 + \frac{\partial u}{\partial x}\frac{\partial v}{\partial y} + \left(\frac{\partial v}{\partial y} \right)^2 + \frac{1}{4}\left[\left(\frac{\partial u}{\partial y} + \frac{\partial v}{\partial x} \right)^2 + \left(\frac{\partial u}{\partial z} + \xi\frac{\partial w}{\partial x} \right)^2 + \left(\frac{\partial v}{\partial z} + \xi\frac{\partial w}{\partial y} \right)^2 \right]. \qquad (27)$$

279 Since (27) differs from (7) only by the incorporation of the continuity equation (22), the

280 transformation leaves both the second invariant $\tilde{\dot{\varepsilon}}^2$ and viscosity $\tilde{\mu}_n$ unchanged, i.e.,

281 $\tilde{\dot{\varepsilon}}^2 = \dot{\varepsilon}^2$ and $\tilde{\mu}_n = \mu_n$. The second invariant remains non-negative, i.e., $\tilde{\dot{\varepsilon}}^2 \geq 0$.

282

283   Boundary conditions for the transformed equations, corresponding to (8)-(12), are

284 given by

285 BCs on S_S:
$$\tilde{\tau}_{ij}n_j - \hat{\xi}\tilde{P}n_i = 0 , \qquad (28)$$

286 BCs on S_{B1}:
$$u_i = 0 , \qquad (29)$$

287 BCs on S_{B2}:
$$u_i n_i = 0 , \qquad (30)$$

288
$$\tilde{\tau}_{(i)j}n_j - \tilde{\tau}_n n_{(i)} + \beta(x)u_{(i)} = 0 , \qquad (31)$$

289 where $\tilde{\tau}_n = n_i\tilde{\tau}_{ij}n_j$ as before. Equations (30), (31) constitute the required three frictional

290 sliding boundary conditions.

291

292   As mentioned, dummy variables $\xi, \hat{\xi}$ in (23)-(25), (27), and (28) are used to

293 identify terms that are neglected in the two types of the Blatter-Pattyn approximation

294 discussed in §3.4. These are (a) the standard Blatter-Pattyn approximation, $\xi = 0, \hat{\xi} = 0$,

295 as originally derived (Blatter, 1995; Pattyn, 2003; DPL, 2010), which solves for just the

296 horizontal velocity components u, v, and (b) the extended Blatter-Pattyn approximation,

297 $\xi = 0, \hat{\xi} = 1$, described more fully later, that contains the standard approximation plus

298 additional equations that determine the vertical velocity w and the pressure $\tilde{P}$. Keeping

299 all terms, i.e., $\xi = 1, \hat{\xi} = 1$, specifies the full transformed Stokes model.

300

301   The transformed system, (23)-(31), and the standard Stokes system, (2)-(12), yield

302 exactly the same solution. However, in common with the Blatter-Pattyn approximation,

303   the transformed system must use a gravity-oriented coordinate system because of the

304   particular type of gravitational forcing being used, while the standard Stokes model is not

305   similarly restricted. This is not a major limitation. A somewhat more restrictive

306   limitation is the appearance of $z_s(x,y)$, an implicitly single valued function, to describe

307   the vertical position of the upper surface of the ice sheet. This means that care must be

308   taken with reentrant upper surfaces (i.e., S-shaped in 2D) and sloping cliffs at an ice

309   edge, again a restriction that is not present in the standard Stokes model. As noted

310   previously, we assume that there is just one upper and one basal surface, i.e., as usual in

311   ice sheet modeling we do not permit overhangs.

312

313   **3.3 The Transformed Stokes Variational Principle**

314

315   It is easy to verify that the transformed Stokes system (23)-(31) results from the variation

316   with respect to $u_i, \tilde{P}$ of the following functional:

317

$$\tilde{\mathcal{A}}[u_i,\tilde{P}] = \int_V dV \left[\frac{4n}{n+1}\eta_0\left(\tilde{\dot{\varepsilon}}^2\right)^{(1+n)/2n} - \hat{\xi}\tilde{P}\frac{\partial u_i}{\partial x_i} + \rho g u_{(i)}\frac{\partial z_s}{\partial x_{(i)}} \right]$$
$$+ \frac{1}{2}\int_{S_{B2}} dS\,\beta(x)\left(u_{(i)}u_{(i)} + \left(u_{(i)}n_{(i)}/n_z\right)^2 \right), \tag{32}$$

318   where $\tilde{\dot{\varepsilon}}^2$ is the transformed second invariant, (27). As in functional (15), basal

319   boundary conditions are imposed by direct substitution. However, boundary conditions

320   using Lagrange multipliers as in (14) are also possible.

321

322   **3.4 Two Forms of the Blatter-Pattyn Approximation**

323   **3.4.1 The Standard Blatter-Pattyn Approximation**

324

325   The standard Blatter-Pattyn approximation (originally introduced by Blatter, 1995,

326   Pattyn, 2003; later by DPL, 2010; Schoof and Hewitt, 2013) is obtained by setting

327     $\xi = \hat{\xi} = 0$ in the transformed system. This yields the Blatter-Pattyn variational,

328

$$\mathcal{A}_{BP}[u_{(i)}] = \int_V dV \left[\frac{4n}{n+1}\eta_0\left(\dot{\varepsilon}_{BP}^2\right)^{(1+n)/2n} + \rho g u_{(i)}\frac{\partial z_s}{\partial x_{(i)}} \right]$$
$$+ \frac{1}{2}\int_{S_{B2}} dS\,\beta(x)\left(u_{(i)}u_{(i)} + \varsigma\left(u_{(i)}n_{(i)}/n_z\right)^2 \right), \tag{33}$$

329   and the second invariant $\dot{\varepsilon}^2_{BP}$, as follows

330
$$\dot{\varepsilon}^2_{BP} = \left(\frac{\partial u}{\partial x}\right)^2 + \frac{\partial u}{\partial x}\frac{\partial v}{\partial y} + \left(\frac{\partial v}{\partial y}\right)^2 + \frac{1}{4}\left[\left(\frac{\partial u}{\partial y} + \frac{\partial v}{\partial x}\right)^2 + \frac{\partial u}{\partial z}^2 + \frac{\partial v}{\partial z}^2\right],$$
(34)

331   in terms of horizontal velocity components u, v only. The Euler-Lagrange equations and

332   boundary conditions are given by

333
$$\frac{\partial \tau^{BP}_{(i)j}}{\partial x_j} - \rho g \frac{\partial z_s}{\partial x_{(i)}} = 0; \quad \begin{cases} \tau^{BP}_{(i)j}n_j + \beta(x)\left(u_{(i)} + \zeta\left(u_{(j)}n_{(j)}/n_z\right)n_{(i)}/n_z\right) = 0 \\ \text{on } S_{B2}, \quad \tau^{BP}_{(i)j}n_j = 0 \text{ on } S_S, \quad u_{(i)} = 0 \text{ on } S_{B1}, \end{cases}$$
(35)

334   where the Blatter-Pattyn stress tensor $\tau^{BP}_{(i)j}$ is

335
$$\tau^{BP}_{(i)j} = \eta_0\left(\dot{\varepsilon}^2_{BP}\right)^{(1-n)/2n}\begin{bmatrix} 2\left(2\dfrac{\partial u}{\partial x} + \dfrac{\partial v}{\partial y}\right) & \left(\dfrac{\partial u}{\partial y} + \dfrac{\partial v}{\partial x}\right) & \dfrac{\partial u}{\partial z} \\ \left(\dfrac{\partial u}{\partial y} + \dfrac{\partial v}{\partial x}\right) & 2\left(\dfrac{\partial u}{\partial x} + 2\dfrac{\partial v}{\partial y}\right) & \dfrac{\partial v}{\partial z} \end{bmatrix}.$$
(36)

336   Equations (35), (36) correspond to (23) and (25) in the transformed Stokes system. A

337   new dummy variable ζ has been introduced in (33) to identify the basal boundary term

338   normally dropped in the standard Blatter-Pattyn approximation $(\zeta = 0)$ but which was

339   restored $(\zeta = 1)$ in Dukowicz et al. (2011) to better represent arbitrary basal topography.

340

341   The Blatter-Pattyn model solves for the horizontal velocity components only. If

342   desired, the vertical velocity component w may in principle be computed a posteriori by

343   means of the continuity equation. Finally, it is important to point out that the Blatter-

344   Pattyn system is numerically well behaved because the variational formulation amounts

345   to a convex optimization problem whose solution minimizes the functional (33).

346

347   **3.4.2 The Extended Blatter-Pattyn Approximation**

348

349   A second form of the Blatter-Pattyn approximation is obtained from the transformed

350   variational principle (32) by making the assumption,

351
$$\left\|\frac{\partial w}{\partial x}\right\| \ll \left\|\frac{\partial u}{\partial z}\right\|, \quad \left\|\frac{\partial w}{\partial y}\right\| \ll \left\|\frac{\partial v}{\partial z}\right\|,$$
(37)

352 and therefore neglecting $\partial w/\partial x, \partial w/\partial y$ in the transformed second invariant $\tilde{\dot{\varepsilon}}^2$,

353 consistent with the original small aspect ratio approximation (Blatter, 1995; Pattyn, 2003;

354 DPL, 2010; Schoof and Hindmarsh, 2008). This corresponds to setting $\xi = 0, \hat{\xi} = 1$ in the

355 transformed Stokes model. In other words, we neglect w-velocity gradients but keep the

356 pressure term in the functional. This will be called the extended Blatter-Pattyn

357 approximation (EBP) because, in contrast to the standard Blatter-Pattyn approximation,

358 all the variables, i.e., $u, v, w, \tilde{P}$, are retained. Notably, assumption (37) is equivalent to

359 just setting $w = 0$ in the second invariant $\tilde{\dot{\varepsilon}}^2$ in the transformed Stokes model. This

360 aspect of the transformed Stokes model will be exploited later to obtain approximations

361 that improve on the Blatter-Pattyn approximation. Thus, the extended Blatter-Pattyn

362 functional is given by

363
$$\mathcal{A}_{EBP}[u_i, \tilde{P}] = \int_V dV \left[\frac{4n}{n+1} \eta_0 \left(\dot{\varepsilon}_{BP}^2 \right)^{(1+n)/2n} - \tilde{P} \frac{\partial u_i}{\partial x_i} + \rho g u_{(i)} \frac{\partial z_s}{\partial x_{(i)}} \right]$$
$$+ \frac{1}{2} \int_{S_{B2}} dS \, \beta(x) \left(u_{(i)} u_{(i)} + \varsigma \left(u_{(i)} n_{(i)} / n_z \right)^2 \right),$$
(38)

364 and the Blatter-Pattyn second invariant $\dot{\varepsilon}_{BP}^2$ is given by (34). Taking the variation of the

365 functional, the system of extended Blatter-Pattyn Euler-Lagrange equations and their

366 boundary conditions is given by

367   (1) Variation with respect to $u_{(i)}$ yields the horizontal momentum equation:

368
$$\frac{\partial \tau_{(i)j}^{BP}}{\partial x_j} - \frac{\partial \tilde{P}}{\partial x_{(i)}} - \rho g \frac{\partial z_s}{\partial x_{(i)}} = 0; \quad \begin{cases} \tau_{(i)j}^{BP} n_j - \tilde{P} n_{(i)} = 0 \text{ on } S_S, \quad u_{(i)} = 0 \text{ on } S_{B1}, \\ \tau_{(i)j}^{BP} n_j + \beta(x) \left(u_{(i)} + \varsigma \left(u_{(k)} n_{(k)} / n_z \right) n_{(i)} / n_z \right) = 0 \\ \text{on } S_{B2}, \end{cases}$$
(39)

369 where $\tau_{(i)j}^{BP}$ is given by (36).

370   (2) Variation with respect to w yields the vertical momentum equation:

371
$$-\frac{\partial \tilde{P}}{\partial z} = 0; \quad \tilde{P} n_z = 0 \text{ on } S_S,$$
(40)

372   (3) Variation with respect to $\tilde{P}$ yields the continuity equation:

373
$$\frac{\partial w}{\partial z} + \frac{\partial u_{(i)}}{\partial x_{(i)}} = 0; \quad w = 0 \text{ on } S_{B1}, \text{ or } w = -u_{(i)} n_{(i)} / n_z \text{ on } S_{B2}.$$
(41)

June 20, 2025

374 It is apparent that the vertical momentum equation system (40) is decoupled, yielding

375 $\tilde{P} = 0$ as already shown in §3.1. This effectively eliminates pressure from the horizontal

376 momentum equation (39), making it identical to the standard Blatter-Pattyn system (35),

377 i.e., a decoupled equation for the horizontal velocities $u_{(i)}$. As a result, having obtained

378 the horizontal velocities from (39), the continuity equation (41) may in principle be

379 solved for the vertical velocity w (but see the comments following (42) regarding the

380 discrete case).

381

382   In summary, the extended Blatter-Pattyn model, (39)-(41), is equivalent to the

383 standard Blatter-Pattyn model, (35), for the horizontal velocities, u, v, but it also includes

384 two additional equations that determine the pressure $\tilde{P}$ and the vertical velocity w,

385 which are ignored in the standard Blatter-Pattyn approximation where only the horizontal

386 velocity is calculated. Because of this, we distinguish between the *Blatter-Pattyn model*

387 that solves for just the two horizontal velocities (i.e., the standard Blatter-Pattyn

388 approximation, (35)), and the *Blatter-Pattyn system* that solves for all the variables (i.e.,

389 the extended Blatter-Pattyn approximation, (39)-(41)). Perhaps the main distinction

390 between the two, which may be important in some applications, is that the vertical

391 velocity in the Blatter-Pattyn system is calculated by solving the continuity equation (41)

392 once horizontal velocities u, v are available on the same mesh as the horizontal

393 velocities, while in the Blatter-Pattyn model the calculation of vertical velocity is

394 completely decoupled and may be done on an unrelated mesh. In the continuous case the

395 solution for the vertical velocity can be done using the Leibniz's theorem,

396
$$w(u,v) = w_{z=z_b} - \int_{z_b}^{z} \frac{\partial u_{(i)}}{\partial x_{(i)}} dz' = u_{(i)} \frac{\partial z_b}{\partial x_{(i)}} - \int_{z_b}^{z} \frac{\partial u_{(i)}}{\partial x_{(i)}} dz' = -\frac{\partial}{\partial x_{(i)}} \int_{z_b}^{z} u_{(i)} dz'. \qquad (42)$$

397 Equation (42) may be used as the starting point for discretization. However, in the

398 following we shall instead discretize the continuity equation (41) by the use of special

399 finite element meshes as described in Appendix A.

400

401   Up to now we have only dealt with continuum properties of Stokes-type systems,

402 which are well behaved. However, this may not be so in the discrete case. The solution

403 of the discretized Stokes systems will depend on the choices that are made for the meshes

404 and for the finite elements that are to be used. These issues will be discussed next.

405

June 20, 2025

406 **4. Finite Element Discretization**

407 **4.1 Standard and Transformed Stokes Discretizations**

408

409 In practice, both traditional Stokes and Blatter-Pattyn models are discretized using finite

410 element methods (e.g., Gagliardini et al., 2013; Perego et al., 2012). We follow this

411 practice except that here the discretization starts from the Stokes variational principle.

412 This differs from standard finite element practice that starts from the Stokes equations

413 and converts them into weak (integral) form, which may not be equivalent to a variational

414 principle unless the Galerkin method is used. This has a number of advantages (see §2.3

415 and DPL, 2010). The following is a brief outline of the discretization. Additional details

416 are provided in Appendix A. For simplicity, we confine ourselves to two dimensions

417 with coordinates (x,z) and velocities (u,w). An example of a three-dimensional mesh

418 appropriate for our purpose is discussed in Appendix A. Further, we discuss only the

419 case of direct substitution for basal boundary conditions in the variational functional.

420 Note that remarks in this Section will apply to both the standard and the transformed

421 Stokes models; for example, the discrete pressure variable p may refer to either the

422 standard pressure P or the transformed pressure $\tilde{P}$.

423

424   Consider an arbitrary mesh with a total of $N = n_u + n_w + n_p$ unknown discrete

425 variables at nodal locations $1 \le i \le N$, with n_u horizontal velocity variables, n_w vertical

426 velocity variables, and n_p pressure variables, so that

427 $$V = \left\{V_1, V_2, \cdots, V_N\right\}^T = \left\{\left\{u_1, u_2, \cdots, u_{n_u}\right\}, \left\{w_1, w_2, \cdots, w_{n_w}\right\}, \left\{p_1, p_2, \cdots, p_{n_w}\right\}\right\}^T = \left\{u, w, p\right\}^T \quad (43)$$

428 is the vector of unknown discrete variables that are the degrees of freedom of the model

429 (if using Lagrange multipliers for basal boundary conditions then discrete variables

430 corresponding to λ_z, Λ must be added). Variables are expanded in terms of shape

431 functions $N_i^k(\mathbf{x})$ associated with each nodal variable i in each element k, so that

432 $V^k(\mathbf{x}) = \sum_i V_i N_i^k(\mathbf{x})$ is the spatial variation of variables in element k, summed over all

433 variable nodes located in element k. Shape functions associated with a given node may

434 differ depending on the variable. Substituting into the functional, (15) or (32), integrating

435 and assembling the contributions of all elements, we obtain a discretized variational

436 functional in terms of the nodal variable vectors u, w, p, as follows

June 20, 2025

$$\mathcal{A}(u,w,p)=\sum_{k}\mathcal{A}^{k}(u,w,p), \tag{44}$$

437

438 where $\mathcal{A}^{k}(u,w,p)$ is the local functional evaluated by integrating over element k. Since

439 the term in the functional involving the product of pressure and divergence of velocity is

440 linear in pressure and velocity, and the term responsible for gravity forcing is linear in

441 velocity, the functional (44) may be written in discrete form as follows

$$\mathcal{A}(u,w,p)=\mathcal{M}(u,w)+p^{T}\left(\mathbf{M}_{UP}^{T}u+\mathbf{M}_{WP}^{T}w\right)+u^{T}F_{U}+w^{T}F_{W}, \tag{45}$$

442

443 where the notation from (43) has been used, i.e., $u=\left\{u_{1},u_{2},\cdots,u_{n_{u}}\right\}^{T}$, etc. Parentheses

444 indicate a functional dependence on the indicated variables. Comparison with (15) and

445 (32) indicates that $\mathcal{M}(u,w)\geq 0$ is a highly nonlinear function of the velocity variables

446 u,w, and $\mathbf{M}_{UP}^{T},\mathbf{M}_{WP}^{T}$ are constant $n_{p}\times n_{u}$ and $n_{p}\times n_{w}$ matrices, respectively, arising from

447 the incompressibility constraint. Note that F_{U},F_{W} are constant gravity forcing vectors of

448 dimension n_{u} and $\mathcal{A}(u)=\mathcal{M}(u,w(u))+u^{T}F_{U}+w(u)^{T}F_{W}$, respectively, such that

449 $F_{U}=0, F_{W}\neq 0$ specifies the standard Stokes model, and $F_{U}\neq 0, F_{W}=0$ specifies the

450 transformed Stokes model. The discrete functional $\mathcal{M}(u,w)$ is different but it remains

451 positive-definite in these two cases.

452

453   Variation of the discretized functional corresponds to partial differentiation with

454 respect to each of the discrete variables in the vector V (see (43)). Thus, the discrete

455 Euler-Lagrange equations that correspond to the u-momentum, w-momentum, and

456 continuity equations, respectively, are given by

457
$$R(u,w,p)=\begin{bmatrix}\partial\mathcal{A}(u,w,p)/\partial u\\\partial\mathcal{A}(u,w,p)/\partial w\\\partial\mathcal{A}(u,w,p)/\partial p\end{bmatrix}=\begin{bmatrix}R_{U}(u,w,p)\\R_{W}(u,w,p)\\R_{P}(u,w)\end{bmatrix}=\begin{bmatrix}\mathcal{M}_{U}(u,w)+\mathbf{M}_{UP}p+F_{U}\\\mathcal{M}_{W}(u,w)+\mathbf{M}_{WP}p+F_{W}\\\mathbf{M}_{UP}^{T}u+\mathbf{M}_{WP}^{T}w\end{bmatrix}=0. \tag{46}$$

458 The functionals $\mathcal{M}_{U}(u,w)=\partial\mathcal{M}(u,w)/\partial u$, $\mathcal{M}_{W}(u,w)=\partial\mathcal{M}(u,w)/\partial w$ are nonlinear

459 vectors of dimension n_{u} and n_{w}, respectively. Altogether, (46) is a set of N nonlinear

460 equations for the $p=-M_{WP}^{-1}\left(M_{W}(u,w(u))+F_{W}\right)$ unknown discrete variables V_{i}. As

461 explained previously in the continuum case, all boundary conditions are included in

June 20, 2025

462 functional (45) and therefore they are also incorporated into the discrete Euler-Lagrange
463 equations (46).
464

465   Since the overall system (46) is nonlinear, it is normally solved using Newton-
466 Raphson iteration, expressed in matrix notation as follows

467
$$\mathbf{M}\left(u^{K}, w^{K}\right)\Delta V + R\left(u^{K}, w^{K}, p^{K}\right) = 0 ,\qquad(47)$$

468 where K is the iteration index, $\mathbf{M}\left(u, w\right) = \partial^{2}\mathcal{A}\left(V\right)/\partial V_{i}\,\partial V_{j}$ is a symmetric $N \times N$

469 Hessian matrix, and ΔV is the column vector given by

470
$$\Delta V = \left\{\Delta u, \Delta w, \Delta p\right\}^{T} = \left\{u^{K+1} - u^{K}, w^{K+1} - w^{K}, p^{K+1} - p^{K}\right\}^{T}.$$

471 Given V^{K} from the previous iteration, (47) is a linear matrix equation that is solved at

472 each iteration for the N new variables V^{K+1}. In view of (45) and (46), the Hessian

473 matrix $\mathbf{M}\left(u, w\right)$ may be decomposed into several submatrices as follows

474
$$\mathbf{M}\left(u, w\right) = \begin{bmatrix} \mathbf{M}_{UU}\left(u, w\right) & \mathbf{M}_{UW}\left(u, w\right) & \mathbf{M}_{UP} \\ \mathbf{M}_{UW}^{T}\left(u, w\right) & \mathbf{M}_{WW}\left(u, w\right) & \mathbf{M}_{WP} \\ \mathbf{M}_{UP}^{T} & \mathbf{M}_{WP}^{T} & 0 \end{bmatrix}.\qquad(48)$$

475 Submatrices $\mathbf{M}_{UW}\left(u, w\right) = \partial^{2}\mathcal{M}\left(u, w\right)/\partial u\,\partial w$, etc., depend nonlinearly on M_{WP}, M_{PW}.

476 Thus, $\mathbf{M}_{UU}\left(u, w\right), \mathbf{M}_{WW}\left(u, w\right)$ are square $n_{u} \times n_{u}$, $n_{w} \times n_{w}$ symmetric matrices,

477 respectively, while $\mathbf{M}_{UW}\left(u, w\right)$ is a rectangular Λ matrix since in general n_{u}, n_{w} are not

478 equal. As noted earlier, $\mathbf{M}_{WP}^{T}$ is an $n_{p} \times n_{w}$ matrix that is not square unless λ_{z}.

479

480 **4.2 Blatter-Pattyn Discretizations**

481

482 For completeness, we express the two Blatter-Pattyn approximations from §3.4 in
483 discretized form from §4.1, as follows
484   (1) The standard Blatter-Pattyn model from §3.4.1 takes the simple form

485
$$R_{U}\left(u, 0, 0\right) = \mathcal{M}_{U}\left(u, 0\right) + F_{U} = 0 ,\qquad(49)$$

486 whose Newton-Raphson iteration is given by

487
$$\mathbf{M}_{UU}\left(u^{K}, 0\right)\Delta u + R_{U}\left(u^{K}, 0, 0\right) = 0 .\qquad(50)$$

488   (2) The extended Blatter-Pattyn approximation from §3.4.2 becomes

489
$$R\left(u,w,p\right)=\begin{bmatrix} \mathcal{M}_U\left(u,0\right)+\mathbf{M}_{UP}p+F_U \\ \mathbf{M}_{WP}p \\ \mathbf{M}_{UP}^T u+\mathbf{M}_{WP}^T w \end{bmatrix}=0\,, \tag{51}$$

490   with the Newton-Raphson iteration given by

491
$$\mathbf{M}\left(u^K\right)\Delta U^{K+1}+R\left(u^K,w^K,p^K\right)=0\,, \tag{52}$$

492   and where the associated Hessian matrix is

493
$$\mathbf{M}\left(u\right)=\begin{bmatrix} \mathbf{M}_{UU}\left(u,0\right) & 0 & \mathbf{M}_{UP} \\ 0 & 0 & \mathbf{M}_{WP} \\ \mathbf{M}_{UP}^T & \mathbf{M}_{WP}^T & 0 \end{bmatrix}. \tag{53}$$

494

495   **4.3 Discrete Solvability Issues**

496   **4.3.1 Solvability of the Stokes and Blatter-Pattyn Models**

497

498   We now consider the solution of the three linear matrix problems $(47),(50),(52)$

499   associated with the Newton-Raphson solution of the Stokes and the Blatter-Pattyn

500   approximate models. While there are no issues in the continuous case, this is not so in

501   the discrete case as noted earlier. The discrete system to be solved has the general form

502
$$\mathbf{M}\begin{Bmatrix} \mathbf{u} \\ p \end{Bmatrix}=\begin{bmatrix} \mathbf{A} & \mathbf{B}^T \\ \mathbf{B} & 0 \end{bmatrix}\begin{Bmatrix} \mathbf{u} \\ p \end{Bmatrix}=\begin{Bmatrix} \mathbf{f} \\ g \end{Bmatrix}, \tag{54}$$

503   where $\mathbf{A}$ is a symmetric, positive definite, invertible matrix, and the variables $\mathbf{u},p$ refer

504   to the Newton-Raphson variable increments. The form (54) is characteristic of Stokes-

505   type problems, or more generally of constrained minimization problems using Lagrange

506   multipliers. In finite element terminology these are called "mixed" problems, meaning

507   that velocity components and the pressure occupy different finite element spaces, or

508   "saddle point" problems, meaning that the solution of (54) is at a saddle point with

509   respect to the velocity and pressure variables of the quadratic form associated with (54).

510   The matrix $\mathbf{M}$ is symmetric but indefinite, with n_u+n_w positive and n_p negative

511   eigenvalues. Some discretizations of this type create matrices whose solution may lack

512   stability (Auricchio et al., 2017). The common way to resolve this is to require the use of

513   finite elements that satisfy the Ladyzhenskaya–Babuška–Brezzi (LBB, or inf-sup)

June 20, 2025

514   condition on matrix $\mathbf{B}^T$ in (54). There is a very large literature on the subject, e.g., Boffi

515   et al. (2008), Elman et al. (2014), Auricchio et al. (2017). Testing for stability is not

516   trivial. However, collections of inf-sup stable elements for the Stokes equations may be

517   found in many papers and books on mixed methods, e.g., Boffi et al. (2008). The popular

518   second-order Taylor-Hood P2-P1 element (Hood and Taylor, 1973) is an example of an

519   inf-sup stable element. Some results using this element are shown in Fig. 13 for Test B,

520   one of the test problems described in Appendix C.

521

522   The two Blatter-Pattyn models are not saddle point problems. The standard

523   Blatter-Pattyn model, (49),(50) eliminates $\mathbf{B},\mathbf{B}^T$ and solves only the positive-definite

524   matrix $\mathbf{A}$, thus making it a well-behaved unconstrained minimization problem. The

525   extended Blatter-Pattyn model, (51),(52), retains the standard form (54) but experiences

526   a different problem because the matrices $\mathbf{M}_{WP}$ and $\mathbf{M}_{WP}^T$ are usually not square and

527   therefore not invertible. Solution for the discrete velocities and pressure as in §3.4.2 in

528   the continuous case is only possible when these two matrices are invertible, which at

529   minimum requires a square matrix, i.e., $n_p = n_w$, and this depends on the finite element

530   mesh chosen for the discretization. For example, the Taylor-Hood (P2-P1) element

531   mentioned previously cannot be used because it typically has $n_p \ll n_w$ and therefore the

532   linear system is overdetermined for the pressure and underdetermined for the horizontal

533   velocity w.

534

535   In the following section we introduce an alternative method for obtaining well-

536   posed formulations of these models, including the extended Blatter-Pattyn model

537   discussed above, by the use of meshes that permit inverting the continuity equation for

538   the vertical velocity in terms of the horizontal velocity components.

539

540   **4.3.2 A Special Case: Invertible Continuity Equation**

541

542   In the continuous case, the Blatter-Pattyn approximation (§3.4) implies that vertical

543   velocity w is obtainable from the continuity equation after having solved for the

544   horizontal velocities u,v. This is always possible in the continuum but it may not be

545   possible in the discrete case, as noted in connection with the extended Blatter-Pattyn

546   approximation and as further explained next. Continuing with the 2D case from §4.1 for

547   simplicity, the discrete continuity equation from (46) or (51) is given by

June 20, 2025

548
$$\mathbf{M}_{UP}^T u + \mathbf{M}_{WP}^T w = 0 \ . \tag{55}$$

549 For this to be solvable for w in terms of the horizontal velocity requires that matrix $\mathbf{M}_{WP}^T$

550 be invertible, i.e., square and full rank. With an invertible matrix, solving (55) we obtain

551
$$w(u) = -\mathbf{M}_{WP}^{-T} \mathbf{M}_{UP}^T u \ , \tag{56}$$

552 where $\mathbf{M}_{WP}^{-T}$ is the inverse of $\mathbf{M}_{WP}^T$. Note that

553
$$\mathbf{M}_{WP}^{-T} = \left(\mathbf{M}_{WP}^T \right)^{-1} = \left(\mathbf{M}_{WP}^{-1} \right)^T \tag{57}$$

554 since, if matrix $\mathbf{M}_{WP}^T$ is invertible, then so is its transpose $\mathbf{M}_{WP}$. In general $\mathbf{M}_{WP}^T$ is an

555 $n_p \times n_w$ matrix so, at minimum, we require that

556
$$n_p = n_w \tag{58}$$

557 for solvability. If Lagrange multipliers are to be used, the number of unknown pressures

558 n_p must be augmented by the number of Lagrange multipliers and therefore (58) would

559 become $n_p + n_{\lambda_z} + n_\Lambda = n_w$ (See Appendix A, §A2, for more details). Assuming that we

560 are dealing with reasonable discretizations, we presume that $\mathbf{M}_{WP}^T$ is full rank. In the

561 following, we refer to (58) (or more correctly, to the invertibility of $\mathbf{M}_{WP}^T$) as the

562 solvability condition. In Appendix A we present several meshes and elements that satisfy

563 this condition, including the P1-E0 element that is used in most of the 2D test problems

564 in this paper.

565

566   Invertibility of the continuity equation has several important implications. We

567 noticed earlier that the extended Blatter-Pattyn model does not work with a Taylor-Hood

568 P2-P1 mesh where the solvability condition is not satisfied. However, using a variant of

569 the Taylor-Hood mesh that does satisfy the solvability condition, the P2-E1 mesh

570 illustrated in Fig. 13A, allows this model to work well. Additionally, we find that the

571 solvability condition is a prerequisite for the Stokes approximations discussed in §6.2.

572 However, good approximations of the vertical velocity may already be available in

573 existing codes; for instance, as in MALI (Hoffman et al., 2018), a code based on the

574 Blatter-Pattyn approximation, to obtain the vertical velocity w for the advection of ice

575 temperature (Mauro Perego, private communication).

576

577   The solvability condition can also be used to convert the Stokes variational

578   principle, (15) or (32), from a constrained to an unconstrained minimization problem.

579   Consider the discrete form of the functional given by (45). Using a mesh that satisfies

580   the solvability condition, and assuming that the vertical velocity $w(u)$ from (56) is

581   available, one may substitute it into functional (45). The term involving pressure drops

582   out because continuity is satisfied, and one obtains a functional in terms of horizontal

583   velocity u only,

584
$$\mathcal{A}(u) = \mathcal{M}(u, w(u)) + u^T F_U + w(u)^T F_W \,. \tag{59}$$

585   This now represents an unconstrained minimization problem since the functional

586    $\mathcal{M}(u, w(u))$ is positive semi-definite. Taking the variation with respect to the horizontal

587   velocity variables u, as in §4.1, one obtains the discrete Euler-Lagrange system of

588   equations for finding the minimum,

589
$$\mathcal{M}_U(u, w(u)) - \mathbf{M}_{UP}\mathbf{M}_{WP}^{-1}\mathcal{M}_W(u, w(u)) + \left(F_U - \mathbf{M}_{UP}\mathbf{M}_{WP}^{-1}F_W\right) = 0 \,. \tag{60}$$

590   This is a set of n_u nonlinear equations for the discrete horizontal velocity variables u that

591   is analogous to the standard Blatter-Pattyn problem of §3.4.1, except that here it

592   represents the full Stokes problem. As in the Blatter-Pattyn case, the solution is expected

593   be well behaved and stable. However, the Newton-Raphson iterative solution of (60)

594   involves a dense Hessian matrix that makes the solution very costly and impractical for

595   large problems.

596

597   Perhaps the main reason for the importance of the solvability condition is that it

598   can function as an alternative for the inf-sup condition to ensure solution stability. As

599   explained in Appendix B, solution stability of the saddle point problem (54) is

600   compromised if the matrix $\mathbf{B}^T$ has a non-empty null space, which in turn is related to the

601   pressure solution containing spurious modes. On the other hand, a solution with a mesh

602   that satisfies the solvability condition produces a matrix equation for the pressure that is

603   invertible. This means that a Stokes saddle point problem is well posed when solved on a

604   mesh that satisfies the solvability condition, without the need to satisfy the inf-sup

605   condition.

606

June 20, 2025

607   **5. Comparison of the Standard and Transformed Stokes Models**

608

609   The standard and transformed Stokes models are expected to converge to the same

610   solution. To verify this we do a number of calculations for some 2D test problems based

611   on the ISMIP-HOM benchmark (Pattyn et al, 2008). These tests, Tests B and D*are

612   described in Appendix C. Test B features no-slip boundary conditions on a sinusoidal

613   bed, and Test D* evaluates sliding of the ice sheet along a flat bed in the presence of

614   sinusoidal friction. The tests are discretized using P1-E0 elements on a regular mesh

615   composed of n quadrilaterals in the x-direction and m quadrilaterals in the z-direction,

616   illustrated in Fig. A1, with each quadrilateral divided into two triangles. Results are

617   presented for two domain lengths, $L = 5$ km and 10 km, to test the aspect ratio range

618   where the Blatter-Pattyn model begins to fail. A relatively coarse mesh, i.e., $m = n = 40$,

619   is used, except when we look at convergence with mesh refinement in Fig. 3.
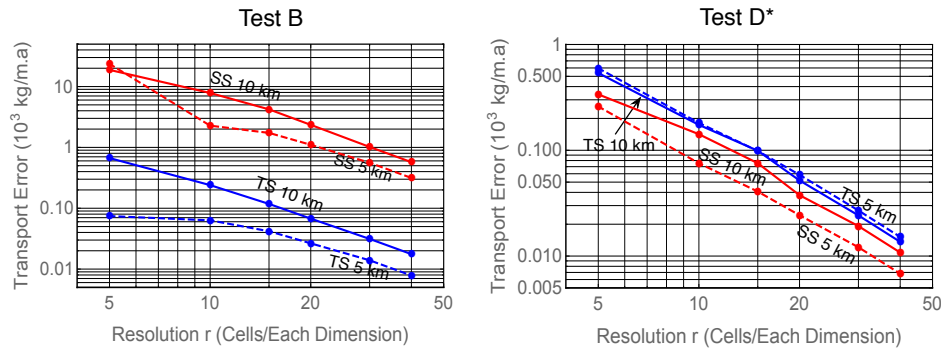
621   **Figure 3.** Convergence of ice transport in Tests B and D* with mesh refinement.

622   Transformed Stokes (TS) plots are in blue and standard Stokes plots (SS) are in red.

623
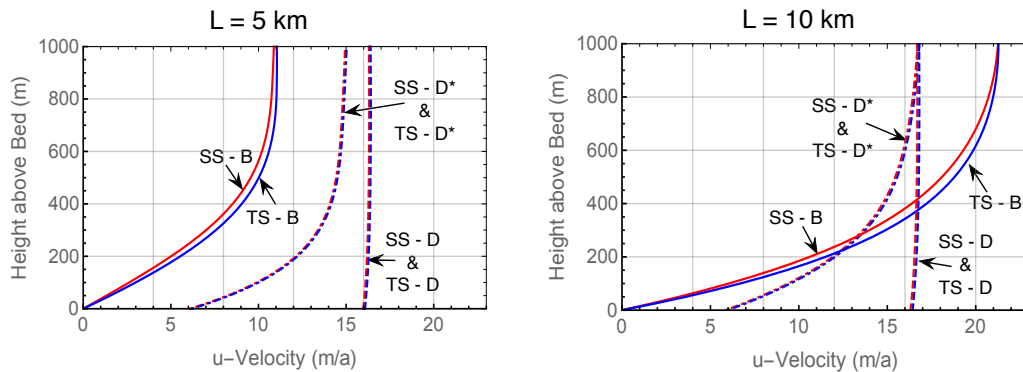
625   **Figure 4.** The u-velocity profile at location $x = L$ as a function of height from the bed.

626

627   Fig. 3 evaluates the convergence of the two Stokes formulations as a function of

628   mesh resolution r, where r is the number of quadrilaterals in either direction. The

June 20, 2025

629   models converge to the same value of the transport, obtained by Richardson

630   extrapolation, and convergence is second order as expected from the use of linear

631   elements. Interestingly, in Test B the transformed Stokes model displays considerably

632   smaller error at all resolutions than the standard model. As a result, the standard Stokes

633   calculations are not fully converged even at the 40x40 resolution. Fig. 4 shows the

634   vertical profiles of the horizontal velocity u at outflow, $x = L$. Results from the no-slip

635   Test B problem and the two frictional sliding problems, Tests D and D*, are plotted. The

636   Test D profile from the ISMIP-HOM benchmark is almost vertically constant, indicating

637   that the value for basal friction that was originally chosen is too small. This motivated

638   the change of Test D to Test D* in Appendix C, with larger basal friction.

639
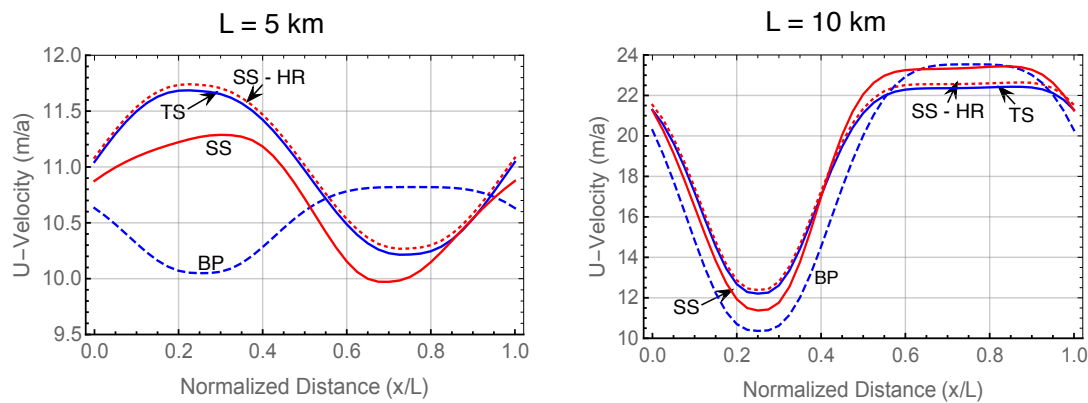
640   **Figure 5.** Upper surface u-velocity, $u\left(x,z_s\right)$ - Test B, No-slip boundary conditions.

641

642
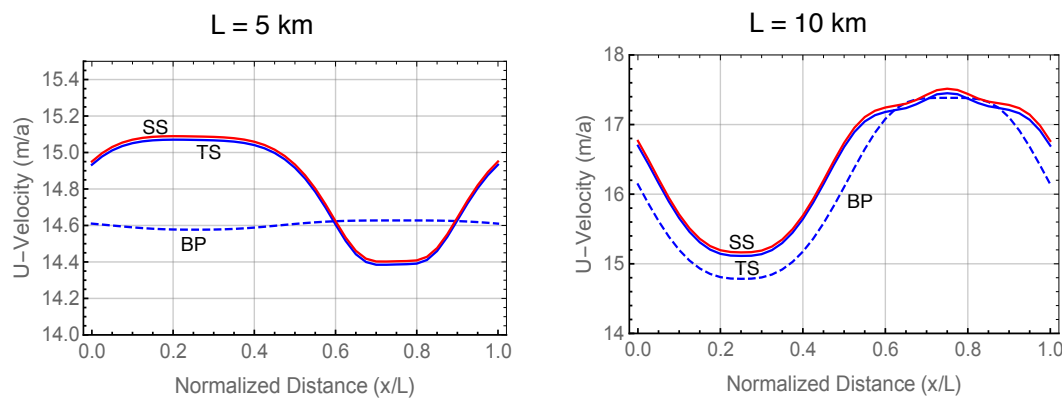
643   **Figure 6.** Upper surface u-velocity, $u\left(x,z_s\right)$ - Test D*, Modified frictional sliding.

644

645   Figs. 5 and 6 show the u-velocity at the ice sheet upper surface for Tests B and

646   D*. This is the benchmark used in ISMIP-HOM to compare different ice sheet models.

647   Four cases are compared: the standard Stokes model (SS), the transformed Stokes model

June 20, 2025

648 (TS), the Blatter-Pattyn (BP) model, and for reference, a very high resolution full-Stokes

649 Test B calculation "oga1" (SS-HR), available from the ISMIP-HOM paper and also

650 independently available in Gagliardini and Zwinger (2008). The TS and the SS-HR plots

651 lie on top of one another (they have been offset slightly for clarity), indicating that the TS

652 model is already fully converged. As before, the SS model is not yet converged in Test

653 B, particularly at $L = 5$ km. As in the ISMIP-HOM study, the Blatter-Pattyn calculation

654 (BP) shows large deviations from the Stokes results, especially so at $L = 5$ km where the

655 surface velocity is entirely out of phase with the Stokes results. Fig. 6 shows that results

656 for the SS and TS models essentially coincide in Test D* (the SS plot has been slightly

657 offset upward for clarity). As expected, Blatter-Pattyn results show noticeable error at

658 $L = 10$ km and very large error at $L = 5$ km. Pressure results have little or no physical

659 significance so they are not presented. However, it was observed that pressures on the

660 P1-E0 mesh were particularly smooth and well behaved.

661

662 **6. Applications of the Transformed Stokes Model**

663 **6.1 Adaptive Switching between Stokes and Blatter-Pattyn Models**

664

665 A way of reducing the cost of a full Stokes calculation is to use it adaptively together

666 with a cheaper approximate model. That is, one may use the cheaper model in those parts

667 of a problem where it is accurate, and the more expensive full Stokes model where the

668 approximate model loses accuracy. One example of such an adaptive approach is the

669 tiling method by Seroussi et al. (2012). However, such methods have drawbacks, such as

670 the need to incorporate two or more presumably quite different models into a single

671 model together with a transition zone to couple the disparate models.

672

673 On the other hand, the transformed Stokes model is particularly simple when used

674 in such an adaptive role because it may be locally switched between the Stokes and

675 Blatter-Pattyn cases simply by switching the parameter $\xi \in \{0,1\}$ on and off. Note that

676 the extended Blatter-Pattyn approximation ($\xi = 0, \hat{\xi} = 1$) needs to be used since then both

677 the Stokes and Blatter-Pattyn parts of the code will have the same number of degrees of

678 freedom. This also implies the use of the P1-E0 mesh since the extended Blatter-Pattyn

679 model requires a mesh satisfying the solvability condition, as explained in §4.3. The

680 extended Blatter-Pattyn approximation is much cheaper than the full Stokes model. For

681 example, the extended Blatter-Pattyn calculation of Test B at a 40x40 resolution as in

682 Figs. 5 and 6 is some 4.3 times cheaper than the corresponding transformed Stokes

June 20, 2025

683 calculation. The standard Blatter-Pattyn approximation ($\xi, \hat{\xi} = 0$) would be somewhat

684 cheaper but it would need more complicated programming, i.e., it would require coupling

685 to the Stokes model with $p = 0$ and $w = w(u,v)$ at the interface between models.

686

687   To demonstrate the idea of adaptive switching with a transformed Stokes model,

688 we introduce a new problem, Test O, described in Appendix C and illustrated in Fig. C1.

689 This consists of an inclined ice slab whose movement is obstructed by a thin obstacle

690 protruding 20% of the ice depth up from the bed. No-slip boundary conditions are

691 applied along the bed and the obstacle. Because of the localized nature of the obstacle,

692 the condition for the validity of the Blatter-Pattyn approximation, (37), must fail near the

693 obstacle and therefore the full Stokes model is needed for good accuracy, at least locally.

694
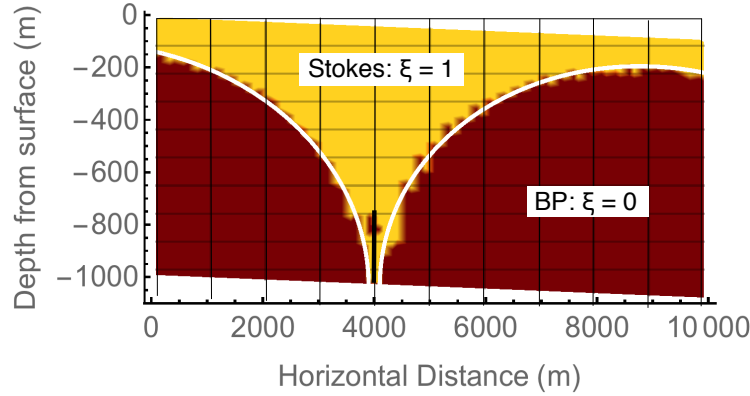
695 **Figure 7.** Mask function (white curve, $z = F_M(x)$) to indicate where the Stokes and BP

696   models are activated in the 20% obstacle test problem. The dark brown region delineates

697   the region where $|\partial w/\partial x| \le 0.1|\partial u/\partial z|$ from a Blatter-Pattyn calculation.

698

699   To implement the method, we first use a Blatter-Pattyn calculation to outline

700 regions where $|\partial w/\partial x| \le 0.1|\partial u/\partial z|$, approximately localizing where the Blatter-Pattyn

701 approximation is valid. This determines a mask function $z = F_M(x)$, illustrated in Fig. 7

702 by the white curves, specifying where the two models must be used. Defining the

703 centroid of a triangular element by (x_C, z_C), the code makes a selection in each element:

704
$$z_C \le F_M(x_C) \quad \Rightarrow \quad \text{Set } \xi = 0, \quad \text{i.e., the Blatter-Pattyn region,}$$
$$z_C > F_M(x_C) \quad \Rightarrow \quad \text{Set } \xi = 1, \quad \text{i.e., the Stokes region.}$$

June 20, 2025

705   The Stokes region occupies the upper part of the domain in Fig. 7 and includes the

706   obstacle, while the Blatter-Pattyn region occupies much of the bottom part of the domain.

707   It is possible to implement a transition zone, e.g., $0 \le \xi(x,z) \le 1$, but this was not done in

708   the present calculation.

709
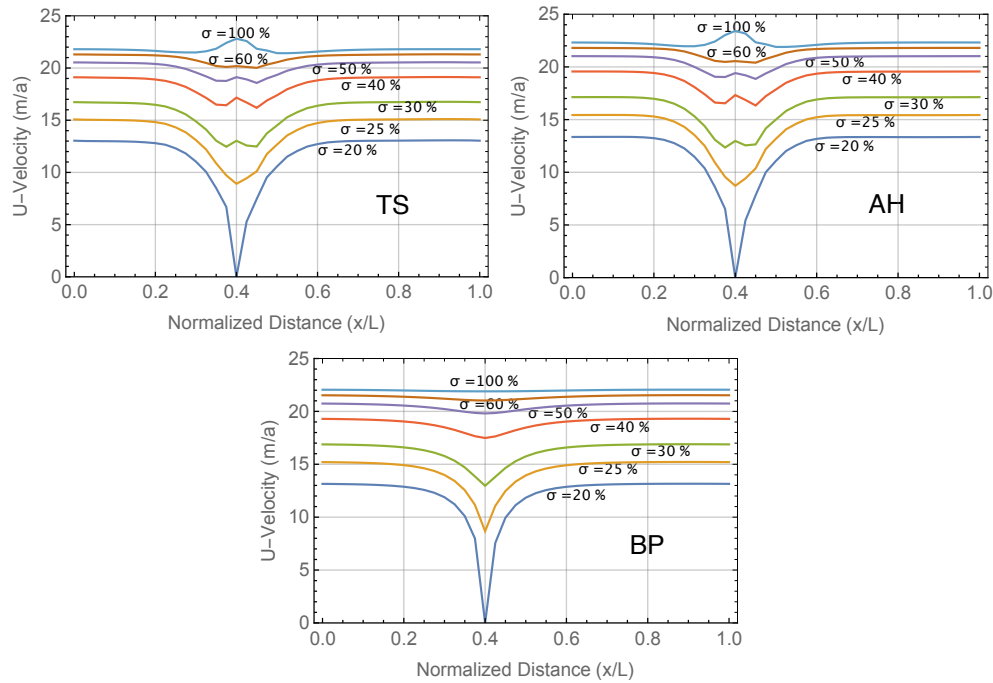
710   **Figure 8.** Horizontal velocity profiles for the Transformed Stokes (TS),

711   the Adaptive-Hybrid (AH), and the Blatter-Pattyn (BP) models in Test O.

712

713   Results from the adaptive-hybrid calculation are shown in Fig. 8, showing curves

714   of the horizontal velocity u at seven different vertical locations specified as a percentage

715   of the distance between top and bottom, with $\sigma = 100\%$ at the top surface. The top right

716   panel shows the results for the adaptive-hybrid calculation (AH), and the top left panel

717   and bottom panel show results for the Stokes (TS) and Blatter-Pattyn (BP) calculations,

718   respectively. All calculations use the 40x40 mesh resolution. The adaptive-hybrid

719   results are very similar to the full Stokes results, reproducing most features of the

720   velocity profiles, including the velocity bump at the top surface, indicating that even the

721   top surface feels the presence of the obstacle. The Blatter-Pattyn results are much less

722   accurate, completely missing the details of the flow near the obstacle. The calculated

723   RMS error relative to the Stokes results in the Blatter-Pattyn case is 0.493 m/a and 0.440

724   m/a in the adaptive-hybrid case. It is larger in the Blatter-Pattyn case, as expected, but

725   the difference is smaller than expected from the visual differences in Fig. 8. Nonetheless,

726   the adaptive-hybrid method must be judged successful if judged by the Fig. 8 results

June 20, 2025

727 alone. As explained later, computational cost comparisons may be misleading and are
728 not provided.
729

730 **6.2. Two New Stokes Approximations**

731

732 As shown in §3.4, simply setting $w = 0$ in the second invariant $\tilde{\varepsilon}^2$ in the transformed

733 functional $\tilde{\mathscr{A}}$ results in the standard Blatter-Pattyn approximation. This suggests that

734 approximating rather than neglecting the vertical velocity w in the functional would

735 create better approximations. We will look at two such methods, although others are

736 possible. The first method, called the Herterich approximation, may be viewed as Picard

737 iteration of the transformed functional (32) where the vertical velocity, obtained from the

738 solution of the continuity equation, is a lagged value from the previous iteration. Two

739 ways of implementing this method are described. The second method, to be called the

740 Dual-Mesh approximation, approximates the vertical velocity by discretizing the

741 continuity equation on a coarser mesh. Since vertical velocity comes from inverting the

742 continuity equation, this has the effect of approximating the vertical velocity and also

743 reducing the number of pressure and vertical velocity variables while preserving the

744 structure of the Stokes model. The degree of approximation is determined by the amount

745 of coarsening of the continuity mesh.

746

747 **6.2.1 The Herterich Approximation**

748

749 Noting that $\tilde{P} = 0$ in the Blatter-Pattyn approximation, we drop the pressure term from

750 the transformed functional (32) and define a new 2D pressure-free functional,

751
$$\tilde{\mathscr{A}}_{PS1}[u] = \int_V dV \left[\frac{4n}{n+1} \eta_0 \left(\tilde{\varepsilon}^2 \right)^{(1+n)/2n} + \rho g u \frac{\partial z_s}{\partial x} \right] + \frac{1}{2} \int_{S_{B2}} dS\, \beta(x) \left(u^2 + \zeta \left(u n_x / n_z \right)^2 \right), \quad (61)$$

752 where

753
$$\tilde{\varepsilon}^2 = \left(\frac{\partial u}{\partial x} \right)^2 + \frac{1}{4} \left(\frac{\partial u}{\partial z} + \frac{\partial w}{\partial x} \right)^2 \qquad (62)$$

754 is the 2D version of the transformed second invariant, (27). Incompressibility must be

755 enforced separately by a second functional,

756
$$\tilde{\mathscr{A}}_{PS2}[p] = \int_V dV\; p \left(\frac{\partial u}{\partial x} + \frac{\partial w}{\partial z} \right). \qquad (63)$$

June 20, 2025

757 Direct substitution is used for boundary conditions in both functionals, as in (15) or (32).

758 Note that functional (61) is a function of u, w but variation is to be taken only with

759 respect to u. Similarly, functional (63) is a function of u, w, p but variation is taken only

760 with respect to p. We are effectively viewing the pressure p as a "test function" in the

761 finite element sense. This gives flexibility to create elements that satisfy the solvability

762 condition (58). For example, in a triangulation some pressures may be assigned to every

763 two triangles, as in a P1-E0 mesh, while others may be assigned to a single triangle so as

764 to achieve an equal number of pressure and vertical velocity variables.

765

766   The variation of $\tilde{\mathcal{A}}_{PS1}[u]$ with respect to u results in a set of n_u discrete Euler-

767 Lagrange equations corresponding to the u-momentum equation,

$$768 \qquad \hat{R}_U(u,w) = \frac{\partial \tilde{\mathcal{A}}_{PS1}(u,w)}{\partial u} = \mathbf{M}_U(u,w) + F_U = 0 . \qquad (64)$$

769 When w is set to zero, this is just the Blatter-Pattyn model, (49). The discrete variation

770 of $\tilde{\mathcal{A}}_{PS2}[p]$ with respect to p, results in the n_p equations of the continuity equation, (55),

$$771 \qquad \hat{R}_P(u,w) = \frac{\partial \tilde{\mathcal{A}}_{PS2}(u,w,p)}{\partial p} = \mathbf{M}_{UP}^T u + \mathbf{M}_{WP}^T w = 0 . \qquad (65)$$

772 These two systems are combined to form the complete system of discrete equations of the

773 Herterich approximation,

$$774 \qquad \hat{R}(u,w) = \left[\hat{R}_U(u,w), \hat{R}_P(u,w) \right]^T = 0 . \qquad (66)$$

775 This is a single system of $n_u + n_p$ equations to determine the $n_u + n_w$ discrete variables

776 u, w, implying that (66) is a viable system for u, w only on meshes satisfying the

777 solvability condition, $n_p = n_w$. Just as in the standard Blatter-Pattyn approximation in

778 §3.4.1, the vertical momentum equation is missing, but here instead of neglecting w, the

779 vertical velocity is obtained consistently from the continuity equation.

780

781   The continuum form of the discrete Euler-Lagrange system (64), (65) is given by

$$782 \qquad \frac{\partial}{\partial x}\left(4\tilde{\mu}\frac{\partial u}{\partial x} \right) + \frac{\partial}{\partial z}\left(\tilde{\mu}\left(\frac{\partial u}{\partial z} + \frac{\partial w}{\partial x} \right) \right) - \rho g \frac{\partial z_s}{\partial x} = 0, \qquad \frac{\partial u}{\partial x} + \frac{\partial w}{\partial z} = 0, \qquad (67)$$

783 along with the boundary conditions,

June 20, 2025

$$4\tilde{\mu}\frac{\partial u}{\partial x}n_x + \tilde{\mu}\left(\frac{\partial u}{\partial z}+\frac{\partial w}{\partial x}\right)n_z = 0 \text{ on } S_S, \quad u=w=0 \text{ on } S_{B1},$$

784

(68)

$$4\tilde{\mu}\frac{\partial u}{\partial x}n_x + \tilde{\mu}\left(\frac{\partial u}{\partial z}+\frac{\partial w}{\partial x}\right)n_z + \beta(x)\left(u+\zeta u\left(n_x/n_z\right)^2\right)=0, \quad w=-u\,n_x/n_z, \Bigg\} \text{ on } S_{B2},$$

785 where the viscosity is $\tilde{\mu}=\eta_0\left(\tilde{\dot{\varepsilon}}^2\right)^{(1-n)/2n}$ as in (26). Remarkably, this same model was

786 introduced by Herterich (1987) to study the transition zone between an ice sheet and an

787 ice shelf[1]. Thus, it predates the widely used Blatter-Pattyn model by some eight years.

788 Unfortunately, in contrast to Blatter-Pattyn, the Herterich model was not pursued further.

789

790   There are two algorithms for solving the Herterich system (66), as follows

791   (1) Herterich Approximation, Newton/Picard iteration version:

792 If we lag the vertical velocity, i.e., $w^{K+1}=w^K \Rightarrow \Delta w=0$ in the first equation of (70), we

793 obtain a Picard iteration algorithm as follows

Starting from $K=0,$ *c*hoose an initial guess, $u^0 \neq 0, w\left(u^0\right),$

794

Solve: $\mathbf{M}_{UU}\left(u^K,w^K\right)\Delta u + \hat{R}_U\left(u^K,w^K\right)=0,$

$u^{K+1}=u^K+\Delta u, \quad w^{K+1}=w\left(u^{K+1}\right)=-\mathbf{M}_{WP}^{-T}\mathbf{M}_{UP}^T u^{K+1},$

(69)

$K=K+1, \qquad$ Repeat until convergence.

795 Each step of the iteration is inexpensive since it is equivalent to a step of the standard

796 Blatter-Pattyn model, (35). On the other hand, Picard iterations typically converge only

797 linearly. It remains to be seen which version is preferable in practice.

798   (2) Herterich Approximation, Quasi-variational, Newton iteration version:

799 Although a single variational principle does not exist, it is still possible to make use of

800 Newton-Raphson iteration to obtain second order convergence. To do this, we treat (66)

801 as a single multidimensional nonlinear system and solve it using Newton-Raphson

802 iteration as follows, with K the iteration index and $\Delta u, \Delta w$ defined previously,

803

$$\mathbf{M}_{UU}\left(u^K,w^K\right)\Delta u + \mathbf{M}_{UW}\left(u^K,w^K\right)\Delta w + \hat{R}_U\left(u^K,w^K\right)=0,$$
$$\mathbf{M}_{UP}^T u^{K+1} + \mathbf{M}_{WP}^T w^{K+1}=0.$$

(70)

804 where $\mathbf{M}_{UU}\left(u,w\right)=\partial\hat{R}_U\left(u,w\right)/\partial u$ and $\mathbf{M}_{UW}\left(u,w\right)=\partial\hat{R}_U\left(u,w\right)/\partial w$ are the same matrices

805 as appear in (48). Convergence is rapid (quadratic) once in the basin of attraction but

806 each step is more expensive than in the Picard iteration described next. Both versions

---

[1] Reference provided by C. Schoof.

807   depend on an invertible continuity equation to obtain $w = w(u)$. However, vertical

808   velocity w may already be available for the purpose of temperature advection in

809   production code packages.
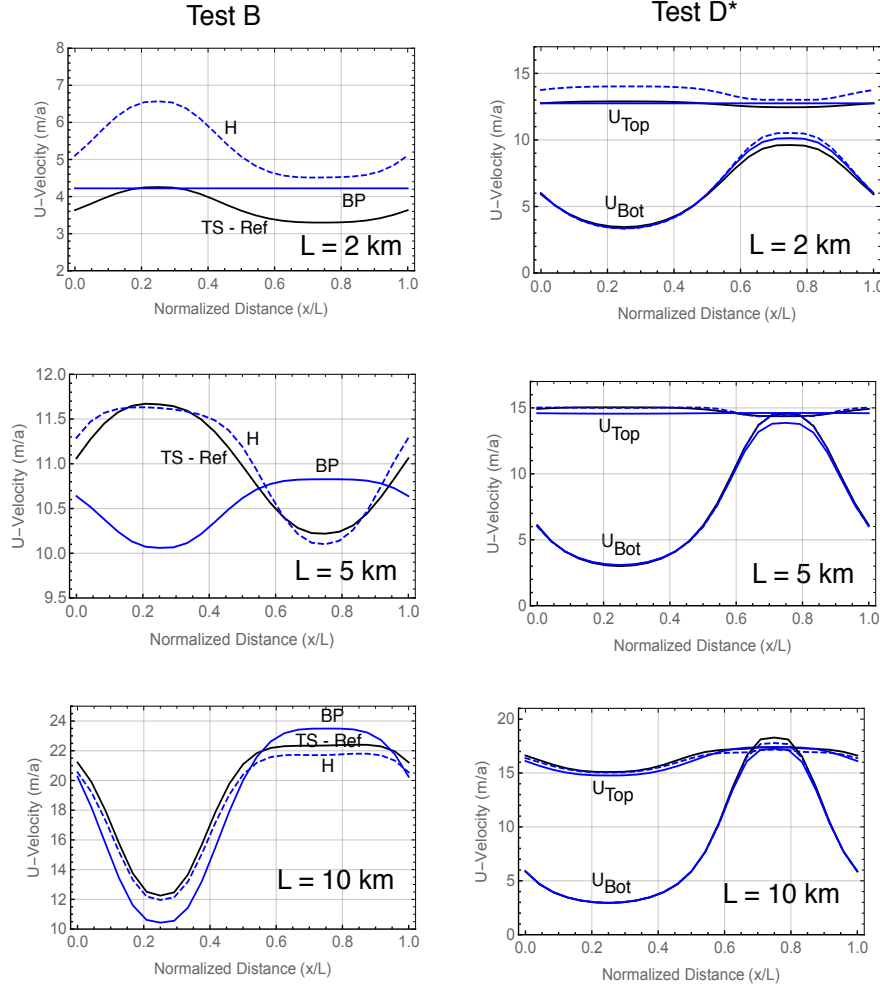
810
811
812   **Figure 9.** Comparing Approximations. Test B, Upper surface u-velocity,

813   and Test D*, Upper and Lower surface u-velocity.

814   TS-Ref: Transformed Stokes; BP: Blatter-Pattyn; H: Herterich.

815   Resolution: 24x24.

816

817   The two Herterich algorithms converge to the same result. Fig. 9 compares the

818   Herterich (H) and the Blatter-Pattyn (BP) approximations to a reference exact

819   transformed Stokes solution (TS-Ref) for Test B results on the left and Test D* results on

820   the right at three problem aspect ratios in the range where small aspect ratio

821   approximation would begin to fail, $\varepsilon = H_0/L = 0.1, 0.2, 0.5$, where $H_0 = 1000\,m$ is the

822   nominal ice thickness and L is the domain length. One might expect the Herterich

823   approximation to be more accurate than the BP approximation since it retains more of the

824   terms from the transformed Stokes model equations than does the Blatter-Pattyn model

825   but this is not borne out in the Fig. 9 results. The Herterich approximation is more

826   accurate in Test B at $L = 5,10\ km$, and this is confirmed by the RMS u-Error results in

827   Fig. 12 where the Herterich model is two to three times more accurate than BP.

828   However, this not the case at $L = 2\ km$ in both Tests B and D*, although Test B results

829   may be deceptive because only the upper surface velocity is displayed (lower surface

830   velocity is zero) and this expands the scale accentuating differences between the three

831   cases. Test D* results are closely clustered except in the $L = 2\ km$ case where,

832   surprisingly, the Herterich approximation is the least accurate. These results cast some

833   doubt on the Herterich approximation, suggesting that it may need to be evaluated

834   further.

835

836   **6.2.2 A "Dual-Mesh" Transformed Stokes Approximation**

837

838   In the Herterich approximation we approximated the vertical velocity directly by lagging

839   w in the second invariant in the variational functional. Here we approximate w

840   indirectly by instead approximating the continuity equation, which determines the

841   vertical velocity. That is, the continuity equation is discretized on a mesh coarser than

842   the one used for the momentum equations. The vertical velocity is then interpolated to

843   appropriate locations on the finer mesh. This reduces the number of unknown variables

844   in the problem, making it cheaper to solve but hopefully without serious loss of accuracy.

845   As described in Appendix C, our test problem meshes are logically rectangular, i.e.,

846   divided into n cells horizontally and m cells vertically. The coarse mesh is constructed

847   by dividing the fine mesh into s equal segments in each direction. This assumes that the

848   integers n and m are each divisible by s, so that there are nm/s^2 coarse cells in total

849   with each coarse cell containing s^2 fine cells. The primary mesh (i.e., the fine mesh) has

850   been chosen to have $n = m = 24$, i.e., a reference 24×24 fine mesh, so as to maximize

851   the number of different coarse meshes available. Coarse meshes were constructed using

852   $s = 2,3,4,6$, and this resulted in fine/coarse mesh combinations labeled by

853   $24 \times 12, 24 \times 8, 24 \times 6, 24 \times 4$, respectively. Similar to a P1-E0 fine mesh, coarse mesh

854   vertical velocities w are located at vertices and pressures at vertical edges. Fig. 10

855   illustrates the case of a single coarse cell and four fine quadrilateral cells for a mesh

856   fragment with $n = m = 2$ and $s = 1$. In the Test B problem with direct substitution for

857   basal boundary conditions there will be nm u-variables and nm/s^2 w- and p-variables

858   each, for a total of $nm\left(1 + 2/s^2\right)$ unknown variables, considerably fewer than the $3nm$

859   variables in the full resolution mesh. The coarse mesh terms in the functional that are

860   affected, $\tilde{P}\left(\partial u/\partial x + \partial w/\partial z\right)$ and $\partial w/\partial x$, are computed by interpolating coarse mesh

861   variables to the fine mesh. We consider two versions of the approximation depending on

862   how the coarse mesh terms are interpolated to the fine mesh.

863
864
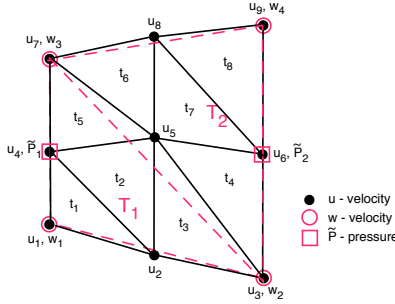
865   **Figure 10.** A Sample of a Coarse/Fine P1-E0 Mesh for the Dual-Mesh Approximation.

866   Resolution: $n = m = 2, s = 1$. Coarse mesh is in red, fine mesh in black.

867

868   (1) Approximation A, Bilinear interpolation:

869   Referring to Fig. 10, the four velocities at the vertices of the coarse mesh

870   quadrilateral, i.e., u_1, u_3, u_7, u_9 and w_1, w_2, w_3, w_4, are used to obtain u, w at the remaining

871   five vertices of the fine mesh by means of bilinear interpolation. Thus, the five velocities

872   u_2, u_4, u_5, u_6, u_8 are obtained in terms of vertex velocities u_1, u_3, u_7, u_9, and similarly for the

873   w velocities. The resulting complete set of fine mesh variables is used calculate the

874   divergence $D = \left(\partial u/\partial x + \partial w/\partial z\right)$ and the quantity $\partial w/\partial x$ in each of the eight triangular

875   elements $t_1, t_2, \cdots, t_8$ of the fine mesh. Coarse mesh pressures $\tilde{P}_1, \tilde{P}_2$ are associated with

876   the coarse mesh triangles T_1, T_2. The products $\tilde{P}_1 D$ in elements t_1, t_2, t_3, t_5 and $\tilde{P}_2 D$ in

877   elements t_4, t_6, t_7, t_8 are then accumulated over the entire mesh to obtain the quantity

878     $\tilde{P}\left(\partial u/\partial x + \partial w/\partial z\right)$ for use in the transformed functional $\tilde{\mathcal{A}}$. Similarly, the quantity

879     $\partial w/\partial x$ is computed in the fine mesh elements from coarse mesh variables for use in the

880   second invariant $\tilde{\dot{\varepsilon}}^2$.

June 20, 2025

881

882 (2) Approximation B, Linear interpolation:

883   In this version, the three velocities at the vertices of the two coarse mesh triangles

884 T_1 and T_2, i.e., u_1, u_3, u_7 and w_1, w_2, w_3 in T_1, and u_7, u_3, u_9 and w_3, w_2, w_4 in T_2,

885 approximate the divergence $D = \left(\partial u / \partial x + \partial w / \partial z \right)$ and $\partial w / \partial x$ as constant values in the

886 two coarse triangles. The constant values $\tilde{P}_1 D$, $\tilde{P}_2 D$ are then accumulated over the

887 entire mesh. The constant value $\partial w / \partial x$ in each coarse triangle is then distributed to each

888 of the eight fine mesh elements $t_1, t_2, \cdots, t_8$, depending on whether the centroid of the fine

889 triangular element is in T_1 or T_2. As in the previous case, this is then used in the second

890 invariant $\tilde{\tilde{\varepsilon}}^2$ in the transformed functional $\tilde{\tilde{A}}$.

891
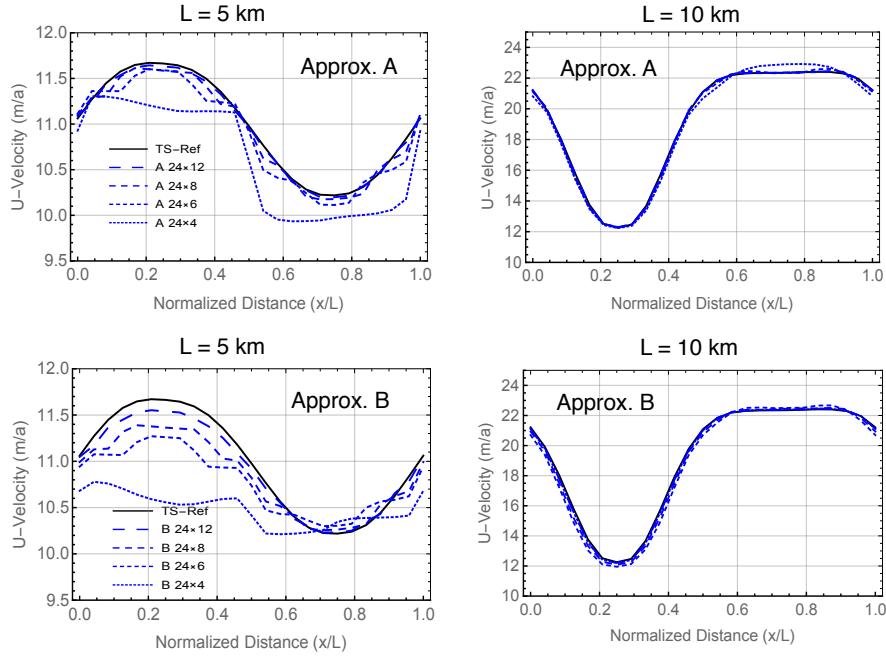
892   **Figure 11.** Comparing Approximations A and B. Test B. Upper surface u-velocity.

893   TS-Ref: Ref. Stokes (r x r = 24x24); Fine/Coarse resolutions (r x R = 24x12, 8, 6, 4).

894

895   While the number and type of unknown variables is the same in the two versions,

896 they differ considerably in accuracy as seen in Figs. 11 and 12. Fig. 11 compares the

897 upper surface u-velocity in approximations A and B, for the five mesh combinations, to

898 the reference 24x24 fine mesh transformed Stokes (TS) calculation. The corresponding

899 Blatter-Pattyn result is shown in Fig. 9. Fig. 12 summarizes and compares the overall

900 accuracy of all approximations by means of the RMS u-Error relative to the TS

June 20, 2025

901   calculation. As might be expected, the accuracy of Approx. A is better than Approx. B,

902   particularly in the case $L = 10$ km. Both dual-mesh versions are more accurate than the

903   BP and H approximations, except for the lowest 24x4 resolution of Approx. B. However,

904   it may be surprising that the SS calculation is the least accurate but this is because SS is

905   not yet fully converged at this resolution (see Fig. 5).

906
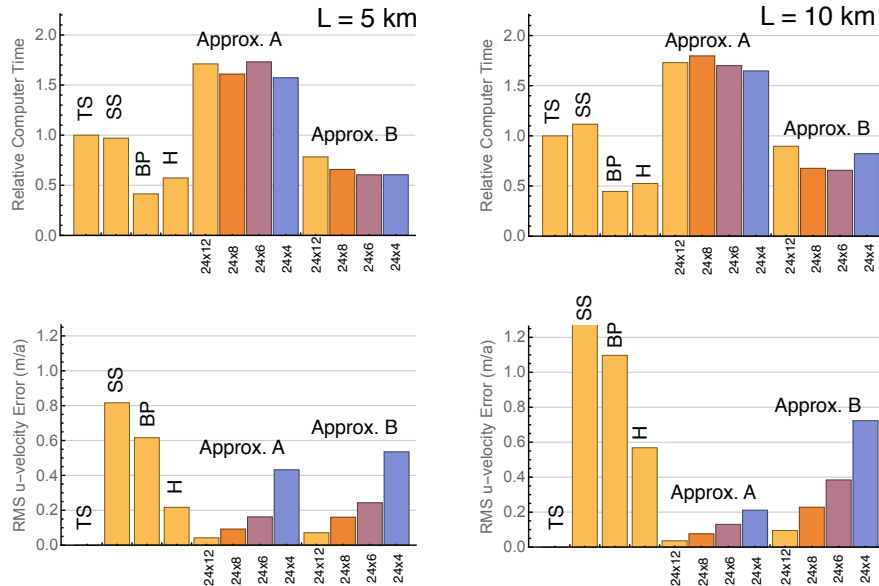
907   **Figure 12.** Comparing the Test B computer time and RMS u-Error results relative

908   to a TS calculation for Approximations BP, H, A, B, and the SS Stokes model.

909   TS, SS, BP, H: Resolution (r x r = 24x24); Approx. A, B: (r x R = 24x12, 8, 6, 4).

910

911   A qualitative comparison of computational time relative to the TS calculation is

912   presented in Fig. 12 for the 24x24 resolution case. The cost of the BP approximation is

913   substantially lower than the cost of full Stokes, while the cost of the Herterich

914   approximation is only slightly higher than BP. This comparison is qualitative and rough

915   because the present calculations are not at all representative of the computer hardware or

916   the methods used in practical ice sheet modeling. The calculations are proof of concept

917   only, made on a personal computer using the program Mathematica, a slow interpreted

918   language. As a result the cost comparisons are inaccurate and possibly misleading. No

919   effort was made to optimize the calculations or to take advantage of parallelization.

920   Thus, for example, the cost of dual-mesh approximations A and B is greatly affected by

921   the cost of the associated interpolations, making them more costly than even the

922   unapproximated calculations, TS and SS. However, the interpolations are highly

923   parallelizable and so would contribute little to the cost in practical computations.

924

925   **7. Second-Order Discretizations**

926

927   So far we have used first-order elements, primarily P1-E0. However, in current practice

928   Stokes models are more often based on second-order elements such as the popular

929   Taylor-Hood P2-P1 element (e.g., Leng et al., 2012; Gagliardini et al., 2013). In 2D the

930   P2-P1 element, illustrated in Fig. 13A, has velocities on element vertices and edge

931   midpoints and pressures on element vertices, resulting in quadratic velocity and linear

932   pressure distributions. This element satisfies the inf-sup stability condition (e.g., Elman

933   et al., 2014) but does not satisfy the solvability condition (58). For example, Test B with

934   direct substitution for basal boundary conditions requires $n_w = 4nm$ vertical velocity

935   variables, many more than the $n_p = n(m+1)$ pressure variables.

936

937   Stokes models work well with a Taylor-Hood mesh as shown in Fig. 13 where

938   both the P2-P1 and P1-E0 models converge to a common Test B solution. Recall that the

939   P2-P1 mesh does not work with the extended Blatter-Pattyn approximation, a model that

940   requires the solvability condition. However, it is possible to construct a second-order

941   element consistent with an invertible continuity equation. This is the P2-E1 element, as

942   illustrated in Fig. 13A. This is second-order for velocities and linear for pressure, just

943   like the P2-P1 element, but the pressure is edge-based rather than vertex-based.

944   Pressures are located midway between velocities along vertical lines, as illustrated in Fig.

945   13A. As explained in Appendix A, this mesh must be constructed using vertical columns

946   of quadrilaterals. Since pressures are vertically collinear with velocities, as in the P1-E0

947   element, the analysis in Appendix A confirms that this element also satisfies the

948   solvability condition (58). A 3D analog exists as is explained in Appendix A.

949

950   Fig. 13B shows the approximate error of the ice transport as a function of mesh

951   refinement for the second-order P2-P1 and P2-E1 meshes in transformed Stokes Test B

952   calculations, together with similar results for the first-order P1-E0 mesh from Fig. 3, for

953   comparison. Note that both second order models show approximately the same error at

954   resolution $r = 16$ as the first order P1-E0 model at resolution $r = 40$, and the same for

955   coarser resolutions such as $r = 8$ and $r = 20$, respectively. However, the second-order

956   calculations are considerably more expensive than the first-order calculations at

957   comparable resolution or accuracy.

June 20, 2025
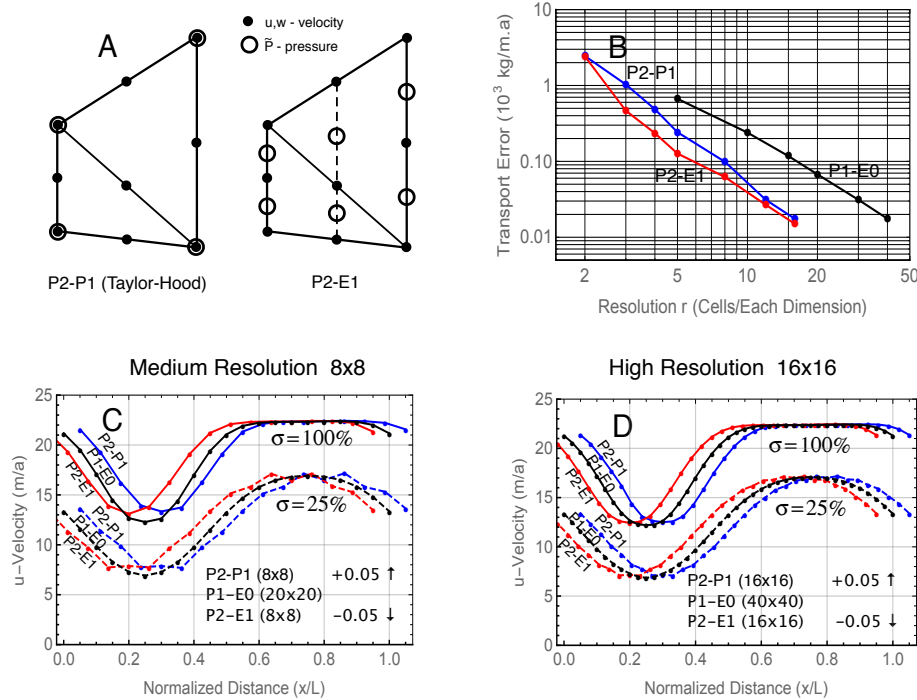
958
959 **Figure 13.** Comparing second-order discretizations based on the P2-P1 and P2-E1
960 elements from panel A to first-order discretizations using the P1-E0 element in Test B
961 calculations with L=10 km. Only transformed Stokes calculations are compared;
962 standard Stokes results behave similarly. Panel B compares the convergence and
963 accuracy of various schemes with increasing resolution, while panels C, D compare
964 horizontal velocities at medium and maximum resolutions.

965

966   Panels C, D in Fig. 13 compare u-velocities from several Test B calculations
967 using the two second-order models to the first-order P1-E0 model results from Fig. 3.
968 Each panel shows upper surface velocities ($\sigma = 100\%$) in solid lines and velocities from
969 a surface a quarter of the way up from the bottom ($\sigma = 25\%$) in dashed lines. Panel C
970 shows medium resolution calculations ($r = 8, 20$ in the second-order and first-order
971 calculations, respectively) and panel D shows higher resolution calculations ($r = 16, 40$).
972 At these resolutions the accuracy of the first- and second-order calculations is very
973 similar so for clarity the second-order results are displaced horizontally from the first-
974 order results by 0.05 nondimensional units. The P2-E1 results in magenta are displaced
975 to the left and the P2-P1 results in blue are displaced to the right. In general, models that
976 satisfy the solvability condition, the P1-E0 and P2-E1 models, are better behaved than the
977 P2-P1 model. This may be related to the well-known "weak" mass conservation of the
978 Taylor-Hood element, which is greatly improved by "enriching" the pressure space with

979   constant pressures in each triangular element (Boffi et al., 2012). Thus, in the 2D Test B

980   problem the pressure variables increase from $n_p = n(m+1)$ in the basic Taylor-Hood

981   element to $n(3m+1)$, much closer to the $4nm$ needed to satisfy the solvability condition.

982   However, pressure in the P2-E1 case is highly oscillatory but well behaved in the P2-P1

983   case. This is consistent with the discussion in Appendix B since the P2-P1 mesh satisfies

984   the inf-sup condition, which is concerned with regularizing the pressure solution (i.e., a

985   condition on the $\mathbf{B}^T$ matrix), while the P2-E1 mesh has no such requirement.

986

987   **8. A Summary and Discussion**

988

989   In summary, this paper presents two innovations in ice sheet modeling. The first involves

990   a transformation of the ice sheet Stokes equations into a form that differs from the

991   approximate Blatter-Pattyn system by a small number of terms. In particular, the

992   variational formulations differ only by the absence of terms involving the vertical

993   velocity w in the second invariant of the strain rate tensor in the Blatter-Pattyn system.

994

995   We focus on two applications of the new transformation, although others may be

996   possible. The first allows these extra terms to be "switched" on or off to convert the code

997   from a full-Stokes model to a Blatter-Pattyn model if desired. Ice sheet flow is generally

998   shallow but often contains limited areas where Stokes equations must be solved. Thus,

999   the switch from Blatter-Pattyn to Stokes may be done locally and adaptively only where

1000   the extra accuracy is required.

1001

1002   The fact that neglecting the vertical velocity in only one localized place creates

1003   the Blatter-Pattyn approximation suggests that an improved approximation will result

1004   from approximating rather than neglecting the vertical velocity. We present two such

1005   approximations but again others may be possible. The first approximation solves the

1006   pressure-free horizontal momentum equation with the vertical velocity obtained from the

1007   continuity equation. This approximation turns out to be the same as a model originally

1008   developed by Herterich (1987). We therefore refer to it as the Herterich approximation.

1009   The second approximation is obtained by discretizing the continuity equation on a coarser

1010   mesh than that used by the rest of the model, which yields an approximate vertical

1011   velocity and thus an approximate Stokes model.

1012

June 20, 2025

1013   The second innovation introduces the use of finite element discretizations that

1014   create a decoupled invertible continuity equation. This allows for the numerical solution

1015   of the vertical velocity in terms of the horizontal velocity components, i.e., $w = w(u,v)$.

1016   These meshes are a prerequisite for the applications mentioned above. Examples of such

1017   meshes for use in 2D and 3D are given in Appendix A, including the P1-E0 mesh that is

1018   used in most of the test problems of this paper. However, perhaps the most important

1019   consequence of this is that invertibility of the continuity equation serves as an alternative

1020   condition for the well posedness of Stokes saddle point problems, as explained in

1021   Appendix B.

1022

1023   **Code Availability**

1024

1025   All calculations were made using the Wolfram Research, Inc. program Mathematica in a

1026   development environment. A large number of Mathematica Notebooks were used to

1027   produce the various results. A representative Notebook (a ,nb file) is available in a public

1028   repository at https://doi.org/10.5281/zenodo.13940989 for a Test $D*$ calculation

1029   (described in Appendix C) at $L = 10 \text{km}$ and a resolution of 20x20. This test problem

1030   was chosen to demonstrate the use of direct substitution for the frictional tangential

1031   boundary condition, (16), in the functional. A Mathematica Notebook may be viewed by

1032   downloading the free Wolfram Player from https://www.wolfram.com/player/. However,

1033   the full Mathematica code is required for editing or execution.

1034

1035   **Competing Interests**

1036

1037   The author has acknowledged that there are no competing interests.

1038

1039   **Acknowledgements**

1040

1041   I am grateful to Steve Price for support, and especially to Mauro Perego, William (Bill)

1042   Lipscomb, and reviewers, particularly Christian Schoof, for comments and suggestions

1043   that helped to improve the paper.

1044

References

Auricchio, F., da Veiga, L.B., Brezzi, F., and Lovadina, C.: Mixed Finite Element Methods, In Encyclopedia of Computational Mechanics Second Edition (Eds E. Stein, R. de Borst, and T.J.R. Hughes), John Wiley & Sons, Ltd., 2017.

Benzi, M., Golub, G.H., and Liesen, J.: Numerical Solution of Saddle Point Problems, Acta Numerica, 14 , 1-137, doi:10.1017/S0962492904000212, 2005.

Blatter, H.: Velocity and Stress Fields in Grounded Glaciers: A Simple Algorithm for Including Deviatoric Stress Gradients, J. Glaciol., 41, 333-344, 1995.

Boffi, D., Brezzi, F., Fortin, M.: Finite Elements for the Stokes Problem. In: Boffi D., Gastaldi L. (eds) Mixed Finite Elements, Compatibility Conditions, and Applications. Lecture Notes in Mathematics, vol 1939. Springer, Berlin, Heidelberg. https://doi.org/10.1007/978-3-540-78319-0_2, 2008.

Boffi, D., Cavallini, N., Gardini, F., and Gastaldi, L.: Local Mass Conservation of Stokes Finite Elements, J. Sci. Comput., 52, 383–400, 2012.

Cheng, G., Lötstedt, P., and von Sydow, L.: A Full Stokes Subgrid Scheme in Two Dimensions for Simulation of Grounding Line Migration in Ice Sheets Using Elmer/ICE (v8.3), Geosci. Model Dev., 13, 2245-2258, 2020.

Colinge, J., and Rappaz, J.: A Strongly Nonlinear Elliptic Problem Arising in a Non-Newtonian Fluid Flow Model in Glaciology, Math. Model. Numer. Anal., 33, 395-406,1999.

Dukowicz, J.K., Price, S.F., and Lipscomb, W.H.: Consistent Approximations and Boundary Condition for Ice Sheet Dynamics from a Principle of Least Action, J. Glaciol., 56, 480-496, 2010.

June 20, 2025

1077 Dukowicz, J.K., Price, S.F., and Lipscomb, W.H.: Incorporating Arbitrary Basal
1078 Topography in the Variational Formulation of Ice Sheet Models, J. Glaciol., 57, 461-467,
1079 2011.
1080
1081 Elman, H.C., Silvester D.J., and Wathen A.J.: Finite Elements and Fast Iterative Solvers:
1082 With Applications in Incompressible Fluid Dynamics, 2nd Ed., Oxford University Press,
1083 494 pp, 2014.
1084
1085 Gagliardini, O., and Zwinger, T.: The ISMIP-HOM Benchmark Experiments Performed
1086 Using the Finite-Element Code Elmer, The Cryosphere, 2, 67–76, 2008.
1087
1088 Gagliardini, O., Zwinger, T., Gillet-Chaulet. F., Durand, G., Favier, L., de Fleurian, B.,
1089 Greve, R., Malinen, M., Martín, C., Råback, P., Ruokolainen, J., Sacchettini, M., Schäfer,
1090 M., Seddik, H., and Thies, J.: Capabilities and Performance of Elmer/Ice, a New-
1091 Generation Ice Sheet Model, Geosci. Model Dev., 6, 1299–1318, doi:10.5194/gmd-6-
1092 1299-2013, 2013.
1093
1094 Glowinski, R. and Rappaz, J.: Approximation of a Nonlinear Elliptic Problem Arising in
1095 a Non-Newtonian Fluid Flow Model in Glaciology, Math. Model. Numer. Anal., 37, 175-
1096 186, 2003.
1097
1098 Greve, R. and Blatter, H.: Dynamics of Ice Sheets and Glaciers, Springer-Verlag, Berlin
1099 Heidelberg, 301 pp, 2009.
1100
1101 Heinlein, A., Perego, M., and Rajamanickam, S.: FROSch Preconditioners for Land Ice
1102 Simulations of Greenland and Antarctica, SIAM J. Sci. Comput., 44, V339-B367, doi:
1103 10.1137/21M1395260, 2022.
1104
1105 Herterich, K.: On the Flow Within the Transition Zone Between Ice Sheet and Ice Shelf,
1106 in Dynamics of the West Antarctic Ice Sheet, Proceedings of a workshop held in Utrecht,
1107 May 6-8, 1985, (Eds. C. J. Van Der Veen and J. Oerlemans), D. Reidel, Dordrecht, 185-
1108 202, 1987.
1109
1110 Hoffman, M. J., Perego, M., Price, S. F., Lipscomb, W. H., Zhang, T., Jacobsen, D.,

1111   Tezaur, I., Salinger, A. G., Tuminaro, R., and Bertagna, L.: MPAS-Albany Land Ice

1112   (MALI): A Variable-Resolution Ice Sheet Model for Earth System Modeling Using

1113   Voronoi Grids, Geosci. Model Dev., 11, 3747–3780, doi:10.5194/gmd-11-3747-2018,

1114   2018.

1115

1116   Hood, P. and Taylor, C.: Numerical Solution of the Navier-Stokes Equations Using the

1117   Finite Element Technique, Comput. Fluids, 1, 1-28, 1973.

1118

1119   Larour, E., Seroussi, H., Morlighem, M., and Rignot, E.: Continental scale, high order,

1120   high spatial resolution, ice sheet modeling using the Ice Sheet System Model (ISSM), J.

1121   Geophys. Res., 117, 1–20, doi:10.1029/2011JF002140, 2012.

1122

1123   Leng, W., Ju, L., Gunzburger, M., Price, S., and Ringler, T.: A Parallel High-Order

1124   Accurate Finite Element Nonlinear Stokes Ice Sheet Model and Benchmark Experiments,

1125   J. Geophys. Res., 117, 2156–2202, doi:10.1029/2011JF001962, 2012.

1126

1127   Lipscomb, W.H., Price, S.F., Hoffman, M.J., Leguy, G.R., Bennett, A.R., Bradley, S.L.,

1128   Evans, K.J., Fyke, J.G., Kennedy, J.H., Perego, M., Ranken, D.M., Sacks, W.J., Salinger,

1129   A.G., Vargo, L.J., and Worley, P.H.: Description and Evaluation of the Community Ice

1130   Sheet Model (CISM) v. 2.1, Geosci. Model Dev., 12, 387-424, 2019.

1131

1132   Nowicki, S.M.J. and Wingham, D.J.: Conditions for a Steady Ice Sheet-Ice Shelf

1133   Junction, *Earth Planet. Sci. Lett.*, **265**(1-2), 246-255, 2008.

1134

1135   Pattyn, F.: A New Three-Dimensional Higher-Order Thermomechanical Ice Sheet

1136   Model: Basic Sensitivity, Ice Stream Development, and Ice Flow across Subglacial

1137   Lakes, J. Geophys. Res., 108(B8), 2382, 2003.

1138

1139   Pattyn, F., Perichon, L., Aschwanden. A., Breuer, B., de Smedt, B., Gagliardini, O.,

1140   Gudmundsson, G.H., Hindmarsh, R.C.A., Hubbard, A., Johnson, J.V., Kleiner, T.,

1141   Konovalov, Y., Martin, C., Payne, A.J., Pollard, D., Price, S., Ruckamp, M., Saito, F.,

1142   Soucek, O., Sugiyama, S., and Zwinger, T.: Benchmark Experiments for Higher-Order

1143   and Full-Stokes Ice Sheet Models (ISMIP–HOM*),* The Cryosphere, 2, 95-108, 2008.

1144

1145   Perego, M., Gunzburger. M., and Burkardt, J.: Parallel Finite-Element Implementation

1146   for Higher-Order Ice-Sheet Models, J. Glaciol., 58, 76-88, 2012.

1147

1148   Rappaz, J., and Reist, A.: Mathematical and Numerical Analysis of a Three-Dimensional

1149   Fluid Flow Model in Glaciology, Math. Model. Mech. Appl. Sci., 15, 37-52, 2005.

1150

1151   Rückamp, M., Kleiner, T., and Humbert, A.: Comparison of ice dynamics using full-

1152   Stokes and Blatter-Pattyn approximation: application to the Northeast Greenland Ice

1153   Stream, The Cryosphere, 16, 1675-1696, 2022.

1154

1155   Schoof, C.: A Variational Approach to Ice Stream Flow, J. Fluid Mech., 556, 227-251,

1156   2006.

1157

1158   Schoof, C.: Coulomb friction and other sliding laws in a higher order glacier flow model,

1159   Math. Models. Meth. Appl. Sci., 20(1), 157–189, 2010.

1160

1161   Schoof, C. and Hewitt, I.: Ice-Sheet Dynamics, Annu. Rev. Fluid Mech., 45, 217–239,

1162   2013.

1163

1164   Schoof, C. and Hindmarsh, R.C.A.: Thin-Film Flows with Wall Slip: An Asymptotic

1165   Analysis of Higher Order Glacier Flow Models, Quart. J. Mech. Appl. Math, 63, *73-114*,

1166   2010.

1167

1168   Seroussi, H., Ben Dhia, H., Morlighem, M., Latour, E., Rignot, E., and Aubry, D.:

1169   Coupling Ice Flow Models of Varying Orders of Complexity with the Tiling Method, J.

1170   Glaciol., 58, 776-786, 2012.

1171

1172   Tezaur, I. K, Perego, M., Salinger, A. G., Tuminaro, R. S., and Price, S. F.:

1173   Albany/FELIZ: A Parallel, Scalable and Robust, Finite Element, First-Order Stokes

1174   Approximation Ice Sheet Solver Built for Advanced Analysis, Geosci. Model Dev., 8,

1175   1197-1220, 2015.

1176

1177 **Appendix A: Meshes that Satisfy the Solvability Condition**
1178 **A1 The P1-E0 Element and the Invertibility of the Continuity Equation**
1179

1180 As discussed in §4, the invertibility of the discrete continuity equation requires special
1181 elements and meshes that satisfy the solvability condition (58). The P1-E0 element,
1182 illustrated in Fig. A1, is one such triangular element that has been used on many
1183 problems in this paper. To work best for the purpose of inverting the continuity equation
1184 for the vertical velocity, i.e., (56), it must be used in a mesh composed of vertical
1185 columns subdivided into triangular elements as shown in a representative mesh in Fig.
1186 A2. Element P1-E0 has velocities located at triangle vertices for a linear velocity
1187 distribution within each triangle (P1), and pressure located on the vertical edge of each
1188 triangle for a constant pressure distribution over the two triangles that share the edge
1189 (E0). A second order version of this element, the P2-E1 element, is shown in Fig. 13A.

1190
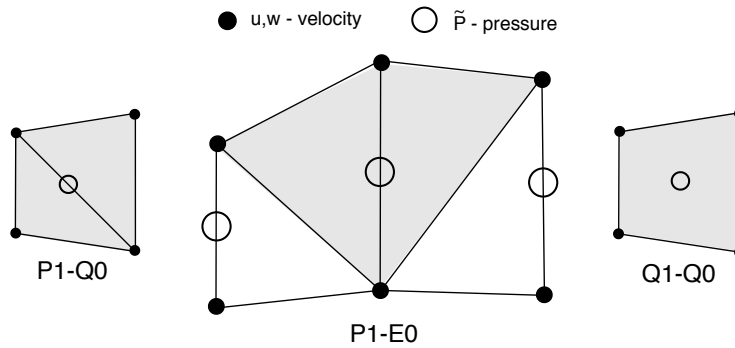
1191 **Figure A1.** The P1-E0 element, and two other secondary 2D elements that satisfy
1192 the solvability condition but possibly only in Tests B and D*.

1193

1194 The triangulation and configuration of pressure basis functions (shown in gray) in
1195 Fig. A2 is quite general except that elements must be arranged in vertical columns, which
1196 still allows for a flexible triangulation of an arbitrary domain. Generally, there are two
1197 triangles associated with a pressure variable, one on each side of a vertical edge, except
1198 where the ice sheet ends at a vertical face, as in Fig. A2. However, this is not a problem
1199 since the pressure is simply associated with the single triangle on one side of the vertical
1200 face. Meshes composed of P1-E0 elements have another useful property. Since pressure
1201 and vertical velocity variables alternate along vertical mesh lines, the matrix-vector
1202 products $\mathbf{M}_{WP}p$, $\mathbf{M}_{WP}^{T}w$ in (46), corresponding to $\partial \tilde{P}/\partial z$ and $\partial w/\partial z$ in the vertical
1203 momentum and continuity equations, respectively, consist of simple decoupled bi-
1204 diagonal one-dimensional difference equations along each vertical mesh line for

1205   determining pressure and vertical velocity. This will be particularly advantageous for
1206   parallelization.
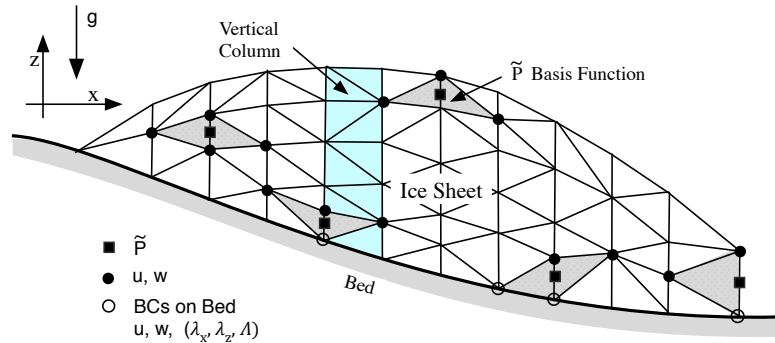
1207
1208   **Figure A2.** An illustration of a 2D edge-based P1-E0 mesh, composed of
1209   vertical columns randomly subdivided into triangles.
1210
1211   The other two elements shown in Fig. A1, the P1-Q0 and Q1-Q0 elements, satisfy
1212   the solvability condition when used in Tests B and D* but possibly not in other problems.
1213   The P1-Q0 element has velocities on triangle vertices for a linear velocity distribution
1214   within each triangle (P1) but pressure is constant within the quadrilateral (Q0) formed by
1215   the two adjoining triangles. The Q1-Q0 element has velocities located at quadrilateral
1216   vertices and pressure centered in the quadrilateral, resulting in a bi-quadratic velocity
1217   distribution (Q1) and a constant pressure within the quadrilateral (Q0). Solutions for all
1218   three elements are stable as expected, and they converge to the same value for ice
1219   transport. The pressure distribution is smooth in the P1-E0 case but contains small
1220   fluctuations near the upper surface in the P1-Q0 and Q1-Q0 cases. These disappear as
1221   resolution is increased. The Q1-Q0 element is unstable in conventional applications
1222   because it contains a checkerboard pressure null space and is only used in a stabilized
1223   form (see Elman et al., 2014, where the element is called Q1-P0). Here, however, it
1224   behaves well perhaps because it satisfies the solvability condition. Overall, this confirms
1225   our expectation of stability when the solvability condition is satisfied.
1226
1227   **A2 Proving the Solvability Condition in P1-E0 Element Meshes**
1228
1229   Consider a single vertical edge from top to bottom as in Fig. A2. Assuming
1230   there are m edge segments in the vertical direction, there will be $m+1$ discrete w
1231   variables and m discrete $\tilde{P}$ variables since each $\tilde{P}$ variable is located between a pair of
1232 w variables. However, since the w variable at the bottom (the bed) is specified as a
1233   boundary condition, either directly as a no-slip condition or as part of a no-penetration

1234   condition, there will be only m unknown w variables. As a result, we have $n_w = n_p$

1235   along each vertical mesh edge and therefore over the entire mesh, thus satisfying the

1236   solvability condition. In case Lagrange multipliers are used, there will be $m+1$ unknown

1237   discrete w variables (since now the basal vertical velocity w is also an unknown).

1238   However, this is matched by m unknown $\tilde{P}$ variables, supplemented by one λ_z or one

1239 Λ unknown Lagrange multiplier variable, depending on the type of boundary condition.

1240   Thus, again the number of unknown variables equals the number of equations along

1241   every vertical edge, thereby satisfying the solvability condition. This means that the P1-

1242   E0 element can be used to satisfy the solvability condition irrespective of the boundary

1243   conditions on quite arbitrary meshes. These arguments apply to other versions of the P1-

1244   E0 element as well, such as the second order version P2-E1 in Fig. 13A or the 3D version

1245   in Fig. A3.

1246

1247   **A3 Three-Dimensional Meshes Based on the P1-E0 Element**

1248

1249   The two-dimensional P1-E0 element has a relatively simple three-dimensional

1250   counterpart, shown in Fig. A3. The mesh again consists of vertical columns, this time

1251   composed of hexahedra. Each hexahedron is subdivided into six tetrahedra such that

1252   each vertical edge is surrounded by as few as four to as many as eight tetrahedra. As in

1253   the 2D case, velocity components are collocated at vertices, yielding a piecewise-linear

1254   velocity distribution in each tetrahedral element, and pressures are located in the middle

1255   of each vertical edge so that pressure is constant in the collection of tetrahedra that

1256   surround that edge. Lagrange multipliers, if used, are located at the vertices on the basal

1257   surface, yielding a piecewise linear distribution on the basal triangular facet. Since

1258   pressures and vertical velocities are again intermingled along a single line of vertical

1259   edges from top to bottom, this satisfies the solvability condition (58) because the

1260   argument used in the 2D case applies here also.

1261

1262   Fig. A3 shows two of the several possible configurations of a typical hexahedron,

1263   including an exploded view of each configuration for clarity. The two configurations

1264   differ in having the internal face of the two forward-facing tetrahedra rotated, creating

1265   two different forward facing tetrahedra. The remaining six tetrahedra are undisturbed.

1266   Since edges must align when hexahedra (or tetrahedra) are connected, this shows that the

1267   3D mesh can be flexibly reconnected and rearranged, just as in the 2D case of Fig. A2.

1268

1269   A closely related and perhaps simpler three-dimensional P1-E0 element is based

1270   on the P2-P1 prismatic tetrahedral element in Leng et al. (2012). A mesh of these

1271   elements is composed of vertical columns of prisms (with triangular faces at the top and

1272   bottom), each subdivided into three tetrahedra. Pressures are located on the vertical

1273   prism edges, as in Fig. A3, so this again satisfies the solvability condition.

1274
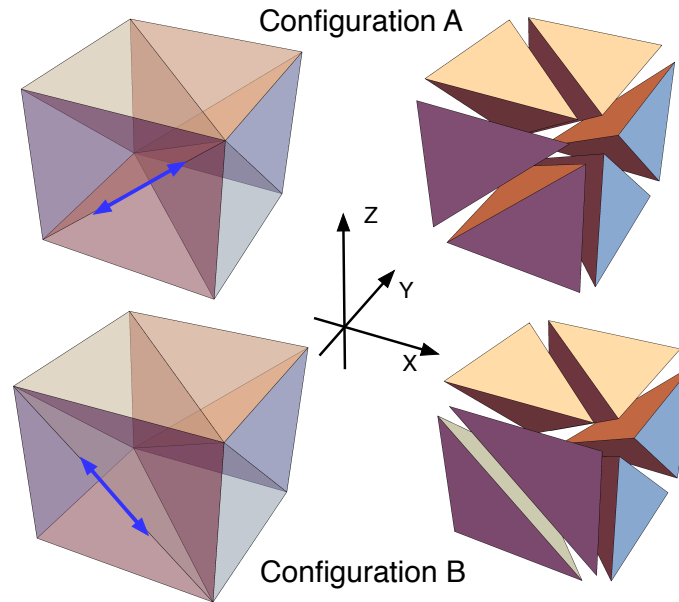
1275   **Figure A3.** Three-dimensional P1-E0 tetrahedral elements that generalize the 2D P1-E0

1276   element of Fig. A1. Configurations A and B differ by having an internal triangular

1277   face rotated, as indicated by the blue arrows. Both satisfy the solvability condition.

1278

1279   Just as the 2D second-order P2-E1 element in Fig. 13A is a generalization of the

1280   P1-E0 element, a 3D second-order P2-E1 element may be constructed as a generalization

1281   of the P1-E0 element in Fig. A3. Velocities would be located at the vertices and at

1282   midpoints of the tetrahedral edges, and pressures halfway between the velocities on

1283   vertical edges, including the imaginary vertical edges through the midpoints of the

1284   tetrahedral edges as in the 2D case in Fig. 13A. The P2-E1 element in both 2D and 3D

1285   satisfies the solvability condition since the arguments of §B2 also apply here as pressures

1286   are located midway between vertical velocities along all vertical edges.

1287

1288 **Appendix B: The Inf-Sup and Solvability Conditions**

1289

1290 Recalling (47), the 2D Newton-Raphson iteration for saddle point problems is written as

1291
$$
\begin{bmatrix}
\mathbf{M}_{UU}\left(u^K, w^K\right) & \mathbf{M}_{UW}\left(u^K, w^K\right) & \mathbf{M}_{UP} \\
\mathbf{M}_{UW}^T\left(u^K, w^K\right) & \mathbf{M}_{WW}\left(u^K, w^K\right) & \mathbf{M}_{WP} \\
\mathbf{M}_{UP}^T & \mathbf{M}_{WP}^T & 0
\end{bmatrix}
\begin{Bmatrix} \Delta u \\ \Delta w \\ \Delta p \end{Bmatrix}
=
\begin{Bmatrix} -R_U\left(u^K, w^K, p^K\right) \\ -R_W\left(u^K, w^K, p^K\right) \\ 0 \end{Bmatrix}. \quad (71)
$$

1292 In the 3D case the vector Δu may stand for the vector of horizontal variable increments,

1293 i.e., $\{\Delta u, \Delta v\}^T$. For simplicity, dropping the Δ's and renaming quantities, (71) is put in

1294 the standard form (54), as follows

1295
$$
\begin{bmatrix} \mathbf{A} & \mathbf{B}^T \\ \mathbf{B} & 0 \end{bmatrix}
\begin{Bmatrix} \mathbf{u} \\ p \end{Bmatrix}
=
\begin{Bmatrix} \mathbf{f} \\ g \end{Bmatrix}, \quad (72)
$$

1296 where $\mathbf{u} = \{u, w\}^T$, $\mathbf{A} = \begin{bmatrix} \mathbf{M}_{UU}\left(u^K, w^K\right) & \mathbf{M}_{UW}\left(u^K, w^K\right) \\ \mathbf{M}_{UW}^T\left(u^K, w^K\right) & \mathbf{M}_{WW}\left(u^K, w^K\right) \end{bmatrix}$, $\mathbf{B} = \begin{bmatrix} \mathbf{M}_{UP}^T & \mathbf{M}_{WP}^T \end{bmatrix}$, etc.,

1297 and the correspondences of the other variables should be obvious.

1298

1299 As noted earlier, matrix $\mathbf{A}$ is invertible. Solving for and eliminating $\mathbf{u}$ in (72),

1300 we obtain an equation for the pressure,

1301
$$
\left(\mathbf{B}\mathbf{A}^{-1}\mathbf{B}^T\right)p = \left(\mathbf{B}\mathbf{A}^{-1}\right)\mathbf{f}, \quad (73)
$$

1302 where $\mathbf{S} = \left(\mathbf{B}\mathbf{A}^{-1}\mathbf{B}^T\right)$ is called the Schur complement with respect to p. This equation

1303 may be solved for p provided an inf-sup condition on matrix $\mathbf{B}^T$ is satisfied (Benzi et

1304 al., 2005; see also the lecture notes by Prof. J-F. Gerbeau for Course CME358, Stanford

1305 University, Chapter 3 (in particular Remarks 3.2 and 3.3), available in:

1306 https://web.stanford.edu/class/cme358/notes/cme358_lecture_notes_3.pdf). Having

1307 solved for p, the velocity $\mathbf{u}$ is given by

1308
$$
\mathbf{u} = \mathbf{A}^{-1}\left(\mathbf{f} - \mathbf{B}^T p\right). \quad (74)
$$

1309 This is generally not a practical solution method since the Schur complement matrix $\mathbf{S}$ is

1310 dense and therefore (73) is too expensive to solve. Gerbeau points out that the standard

1311 inf-sup condition for $\mathbf{B}^T$ is equivalent to the much simpler "algebraic inf-sup condition",

1312
$$Ker\mathbf{B}^T = \{0\} , \tag{75}$$

1313   i.e., the inf-sup condition is the same as requiring that the null space of $\mathbf{B}^T$ be the zero

1314   vector. Furthermore, this means that the inf-sup condition or (75) implies that the

1315   pressure solution must not contain spurious modes. This suggests that the existence of a

1316   pressure null space is the culprit in the need to satisfy the inf-sup condition.

1317

1318   On the other hand, consider the situation when the Newton-Raphson system (71)

1319   is solved with a mesh satisfying the solvability condition. Simplifying notation, the

1320   linear system (71) may be rewritten as follows

1321
$$\begin{bmatrix} \mathbf{M}_{UU} & \mathbf{M}_{UW} & \mathbf{M}_{UP} \\ \mathbf{M}_{UW}^T & \mathbf{M}_{WW} & \mathbf{M}_{WP} \\ \mathbf{M}_{UP}^T & \mathbf{M}_{WP}^T & 0 \end{bmatrix} \left\{ \begin{array}{c} u \\ w \\ p \end{array} \right\} = \left\{ \begin{array}{c} f_U \\ f_W \\ 0 \end{array} \right\} . \tag{76}$$

1322   If the solvability condition applies, the matrices $\mathbf{M}_{WP}, \mathbf{M}_{WP}^T$ are invertible, as before, and

1323   the continuity equation, the third equation from (76), may be solved for the vertical

1324   velocity w as before, as follows

1325
$$w = -\mathbf{M}_{WP}^{-T}\mathbf{M}_{UP}^T u , \tag{77}$$

1326   corresponding to (56). Recall from §4.3.2 that using (56) in functional (59) one obtains

1327   (60), an equation for u only. With a bit of algebra, and now using (77) in (76), the

1328   corresponding linear equation for u is given by

1329
$$\left(\mathbf{M}_{UU} - \left(\mathbf{M}_{UW} - \mathbf{M}_{UP}\mathbf{M}_{WP}^{-1}\mathbf{M}_{WW} \right)\mathbf{M}_{WP}^{-T}\mathbf{M}_{UP}^T - \mathbf{M}_{UP}\mathbf{M}_{WP}^{-1}\mathbf{M}_{UW}^T \right)u$$
$$= \left(f_U - \mathbf{M}_{UP}\mathbf{M}_{WP}^{-1}f_W \right). \tag{78}$$

1330   However, just as was the case with (73), the associated matrix is full and too expensive to

1331   solve in practice. Nevertheless, with u given by (78), one obtains the following matrix

1332   equation from the second equation of (76), to be solved for the pressure p:

1333
$$\mathbf{M}_{WP}p = \left(\mathbf{M}_{WW}\mathbf{M}_{WP}^{-T}\mathbf{M}_{UP}^T - \mathbf{M}_{UW}^T \right)u + f_W . \tag{79}$$

1334   Thus, corresponding to equations (74) and (73), one obtains (78) and (79), but now to be

1335   solved in reverse order, first for velocity u, then for the pressure p. The essential

1336   difference between the equations for the pressure, (73) and (79), is that the Schur

1337   complement matrix $\mathbf{S}$ requires the inf-sup condition to be satisfied, while there is no such

1338   requirement for $\mathbf{M}_{WP}$. Thus, pressure solutions will be well behaved with no spurious

1339   pressure modes, although there is no guarantee or expectation of smoothness. This

June 20, 2025

1340   implies that the solvability condition (58), and more importantly, the invertibility of

1341   matrix $\mathbf{M}_{WP}^{T}$, is sufficient for the well posedness of the Stokes saddle point problem.

1342

1343   **Appendix C: Test Problems**

1344

1345   We use three 2D test problems to demonstrate the new methods. The geometrical

1346   configuration of the three problem meshes is illustrated in Fig. C1. The first problem,

1347   named Test B, is actually Exp. B from the ISMIP-HOM benchmark suite (Pattyn et al.,

1348   2008); it features a no-slip condition on a sinusoidal basal surface. The second problem,

1349   Test D*, incorporates sinusoidal friction along a uniformly sloped plane basal surface.

1350   This is a modification of Exp. D from the benchmark suite with increased friction since

1351   ice flow in Exp. D is very nearly vertically constant (see Fig. 4), which is characteristic of

1352   the shallow-shelf regime and not representative of a more typical flow regime.

1353

1354   A third problem, Test O (for "Obstacle") is introduced to illustrate the adaptive

1355   switching discussed in §6.1. As illustrated in Fig. C1, Test O has a unique feature, a thin

1356   no-slip obstacle, located at $x = 4\,km$ and extending vertically $200\,m$ from the bed (20 %

1357   of the ice sheet thickness), which forces ice flow near the obstacle to adjust abruptly.

1358   However, because of the no-slip boundary conditions along the obstacle surface, the

1359   triangular element in the lee of the obstacle, with one vertical edge and one edge along

1360   the bed, would result in zero vertex velocities. This would imply zero stress and

1361   therefore a singularity in ice viscosity. To avoid this, elements at the back of the obstacle

1362   are "reversed" compared to the ones at the front of the obstacle as shown in Fig. C1.

1363

1364   All tests feature a sloping flat upper surface, given by $z_s(x) = -x\,\mathrm{Tan}(\theta)$, where

1365 $\theta = 0.5°$ for Tests B and O, and $\theta = 0.3°$ for Test D* (this differs from the $0.1°$ slope in

1366   Test D), with free-stress boundary conditions. The bottom surface elevation in Test B is

1367   given by $z_b(x) = z_s(x) - H_0 + H_1\,\mathrm{Sin}(\omega x)$, where the $H_0 = 1000\,m$, $H_1 = 500\,m$,

1368 $\omega = 2\pi/L$, and L is the perturbation wavelength or domain length. The bottom surface

1369   elevation in Tests D* and O is $z_b(x) = z_s(x) - H_0$, which is parallel to the upper surface.

1370   Problem length L in the ISMIP-HOM suite ranges from $5\,km$ to $160\,km$ but here we

1371   consider only three cases at the high end of the aspect ratio (H_0/L) range, namely

June 20, 2025

1372 $L = 2, 5, 10 \, km$, where the inaccuracy of the Blatter-Pattyn approximation becomes

1373   noticeable. Lateral boundary conditions are periodic. The spatially varying friction

1374   coefficient for Test D* is $\beta(x) = \beta_0 + \beta_1 \mathrm{Sin}(\omega x)$, where $\beta_0 = \beta_1 = 10^4 \, Pa \, a \, m^{-1}$ (this is

1375   an order of magnitude larger than in Test D). Physical parameters are the same as in

1376   ISMIP-HOM, i.e., ice-flow parameter $A = 10^{-16} \, Pa^{-3} a^{-1}$, ice density $\rho = 910 \, kg \, m^{-3}$, and

1377   gravitational constant $g = 9.81 \, ms^2$. In general, units are MKS, except usually time is

1378   per annum, convertible to per second by the factor $3.1557 \times 10^7 \, s \, a^{-1}$.
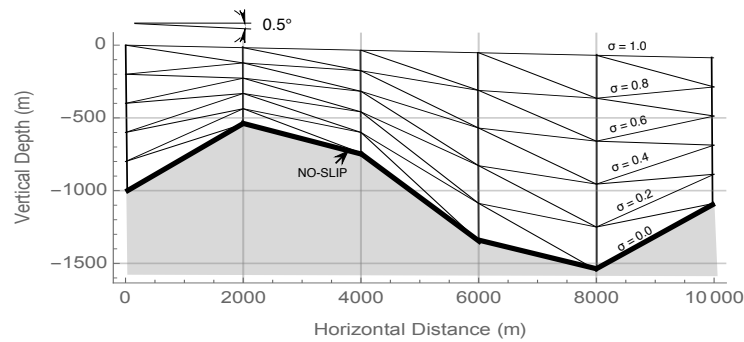
ISMIP-HOM Test Problem B - No Slip
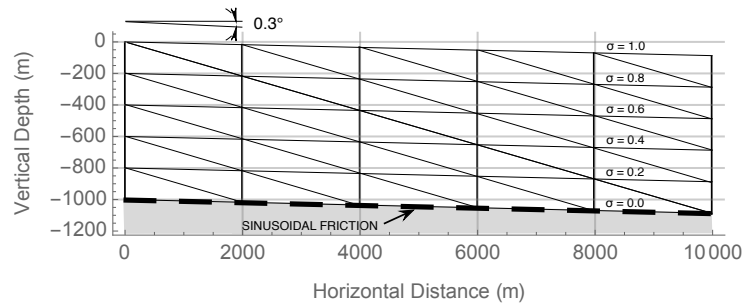
Test Problem D* - Sinusoidal Friction
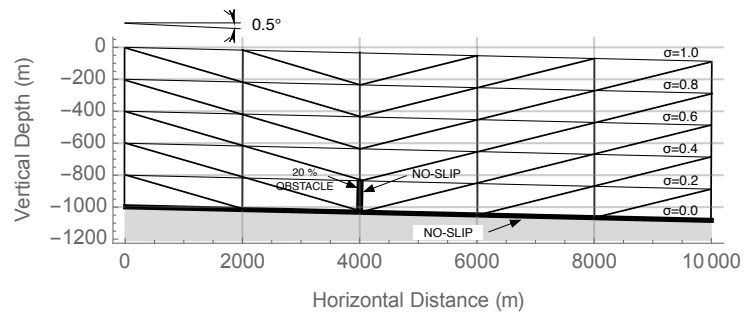
Test Problem O - 20% Obstacle - No Slip

1379

1380   **Figure C1.** Test problem meshes. For clarity, a coarse 5x5 configuration is shown.

June 20, 2025